^{40}Ar/^{39}Ar and U-Pb constraints on the age of the Zaozigou gold deposit, Xiahe-Hezuo district, West Qinling orogen, China: Relation to early Triassic reduced intrusions emplaced during slab rollback

Ji-Xiang Sui[a,b], Jian-Wei Li[a,b,*], Xiao-Ye Jin[b], Paulo Vasconcelos[c], Rui Zhu[d]

[a] State Key Laboratory of Geological Processes and Mineral Resources, China University of Geosciences, Wuhan 430074, China
[b] School of Earth Resources, China University of Geosciences, Wuhan 430074, China
[c] School of Earth Sciences, The University of Queensland, Brisbane, QLD 4072, Australia
[d] Zaozigou Gold Mine, Zhaojin Mining Industry Co. LTD., Hezuo, 747000, China

ARTICLE INFO

ABSTRACT

The West Qinling orogen in central China contains dozens of world-class sediment-hosted gold deposits, but the ages of these deposits and their relation to regional tectonism, magmatism, and metamorphism are poorly understood. Zaozigou, in the western zone of the Xiahe-Hezuo district, is one of the larger deposits in the orogen with 142 t Au at an average grade of 2.69 g/t. It is hosted in a middle Triassic turbidite sequence and swarm of crosscutting ilmenite-series intermediate to felsic dikes. Ore bodies are localized along subvertical, NE- or NS-striking faults. Gold occurs in fine-grained arsenian pyrite and arsenopyrite disseminated in hydrothermally altered sedimentary and igneous rocks and in subordinate sulfide-quartz-ankerite veinlets. Such mineralization is locally crosscut and overprinted by NW-striking, gently-dipping, auriferous stibnite-quartz veins.

Zircon grains from gold mineralized granodiorite and quartz diorite porphyry dikes have U-Pb ages of 248.9 ± 1.4 to 244.8 ± 1.4 Ma, whereas a post-ore diorite porphyry dike has a U-Pb age of 237.5 ± 1.4 Ma. Two samples of sericite associated with disseminated arsenian pyrite and arsenopyrite in sedimentary and igneous host rocks yield plateau ages of 245.6 ± 1.0 Ma and 242.1 ± 1.0 Ma, that are bracketed by the zircon U-Pb ages on pre- and post-ore dikes. Field relationships and geochronological results, thus, constrain magmatism and gold mineralization at the early Triassic.

Previous work has shown that the Au-Cu skarns and intrusion-related gold deposits exposed at a deeper level in the eastern zone of the Xiahe-Hezuo district are genetically related to early-middle Triassic ilmenite series intrusions generated in an extensional back-arc setting during rollback of the subducted paleo-Tethyan slab. Our U-Pb and ^{40}Ar/^{39}Ar data show that the large Zaozigou gold deposit in the western zone of the Xiahe-Hezuo district is broadly coeval with the Au-Cu skarn and intrusion-related gold deposits in the eastern zone. This temporal consistency provides additional support for a genetic link between gold mineralization and magmatism in the Xiahe-Hezuo district. As such, this district may represent the only reduced intrusion related gold system in the West Qinling Orogen.

1. Introduction

The > 1500 km long, WNW-trending West Qinling orogen was generated by subduction and closure of the paleo-Tethys and subsequent continental collision between the South China Block and North China Craton (Fig. 1; Dong et al., 2015, 2011; Zhang et al., 2001, 1996). This orogenic belt is endowed with dozens of world class gold deposits as well as more than 50 smaller ones that constitute the second largest gold province in China (Fig. 1; Chen et al., 2004; Chen and Santosh, 2014; Liu et al., 2015; Mao et al., 2002). Most of the gold deposits are hosted in Cambrian to early Triassic marine sedimentary rocks and have arguably been classified as Carlin-like (Chen et al., 2004; Liu et al., 2015, 1994; Mao et al., 2002) or orogenic gold deposits (Mao et al., 2002). Although most of these gold deposits have been studied for decades, their age, genesis and relation to the geotectonic evolution of the West Qinling orogen remains a matter of debate (Chen and Santosh, 2014; Jin et al., 2017; Liu et al., 2015; Mao et al., 2002; Zeng et al., 2012).
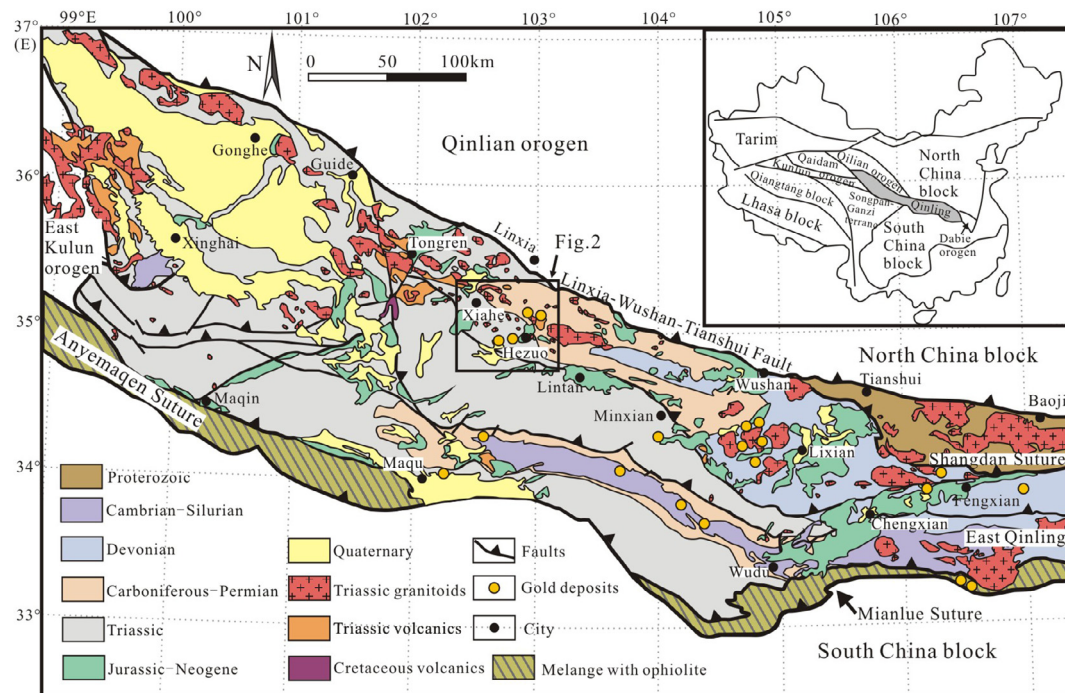
Fig. 1. A. Simplified geologic map of the Qinling orogen showing the distribution of major granitic intrusions and gold deposits (modified from Jin et al., 2017). The insert is the tectonic division of China with location of the Qinling orogen.
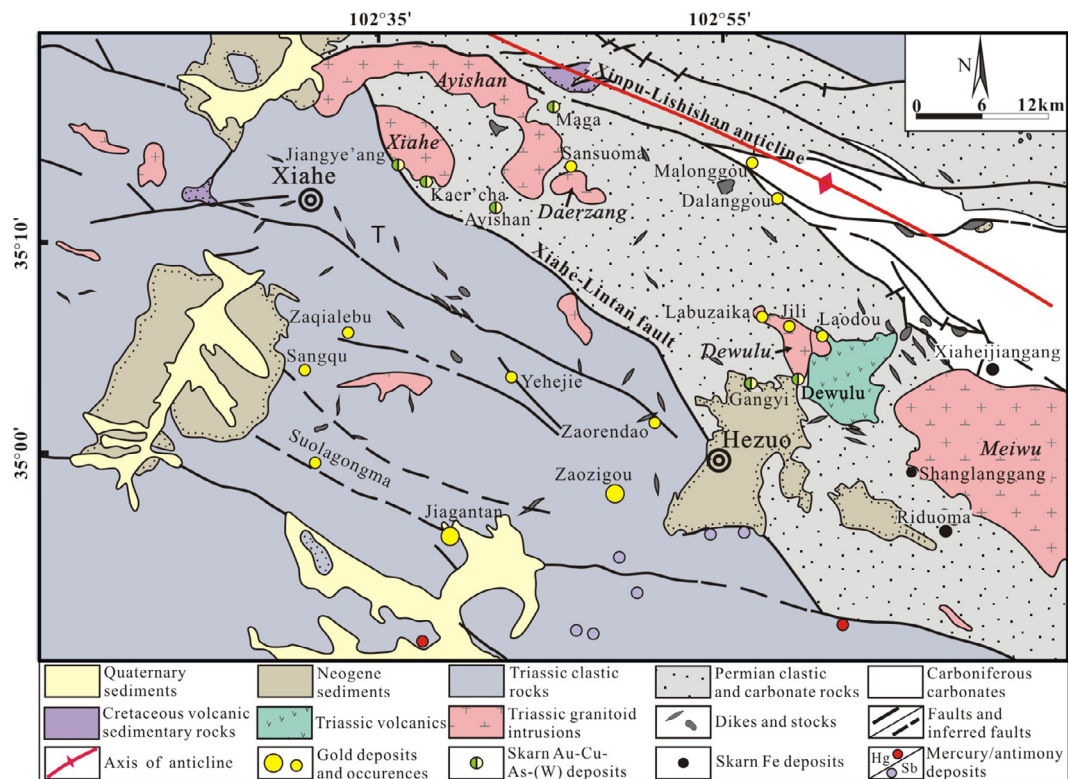

Fig. 2. Geologic map of the Xiahe-Hezuo district showing the distinct geology and styles of gold mineralization in the eastern and western zones separated by the Xiahe-Lintan Fault (after Sui et al., 2017).

The Xiahe-Hezuo district in the western portion of the West Qinling orogen has been a major exploration area over the last decade due to the discovery of several large-tonnage gold deposits, including Zaozigou, Jiagantan, Laodou and Labuzaika (Fig. 2). This district can be divided into eastern and western zones by the NNW-trending Xiahe-Lintan thrust fault (Jin et al., 2017; Liu et al., 2011; Sui et al., 2017; Fig. 2). In the eastern zone, several Au-Cu-(W) skarn deposits occur within or proximal to the early to middle Triassic granitoid intrusions that intruded into the Permian and Carboniferous clastic rocks and carbonates (Fig. 2). The age of the Dewulu Au-Cu skarn deposit has

been precisely constrained at 239.9 ± 1.4 Ma by $^{40}Ar/^{39}Ar$ dating of hydrothermal biotite (Sui et al., 2017). Several Au-As-Sb-Pb-Zn-(Cu) vein deposits are spatially associated with granitoid intrusions, as best illustrated by the Labuzaika, Jili, and Laodou (Fig. 2). Two ore-related sericite samples from Laodou yielded well-defined $^{40}Ar/^{39}Ar$ plateau ages of 249.1 ± 1.6 and 249.0 ± 1.5 Ma (Jin et al., 2017). The western zone is dominated by Triassic flysch sediments that are intruded by a swarm of granitoid dikes. Numerous sediment- and dike-hosted gold deposits have been discovered in the western zone (Cao et al., 2012; Liu et al., 2011), however, their age and relation to magmatism and gold deposits in the eastern zone remains poorly understood.

Zaozigou is the largest gold deposit in the western zone, with proven reserves of 142 tons gold at an average grade of 2.69 g/t (Chen et al., 2011, 2015). Gold mineralization is mostly hosted in hydrothermally altered turbidites, with amounts in intermediate to felsic dikes (Fig. 2). The presence of numerous pre- and post-ore dikes and ore-related sericitic alteration at Zaozigou provides an excellent opportunity to constrain the timing of gold mineralization. In this paper, we present zircon U-Pb ages on pre- and post-ore dikes along with $^{40}Ar/^{39}Ar$ dates on ore-related hydrothermal sericite to constrain the timing of magmatism and hydrothermal activity at Zaozigou. The geochronologic results at Zaozigou are then compared to those from intrusions and gold deposits in the eastern zone and are found to be broadly coeval. Finally, the subduction related tectonic setting responsible for the granitoid intrusions and gold deposits in the Xiahe-Hezuo district is discussed and shown to be distinct from the collisional setting associated with orogenic gold deposits in the West Qinling orogen.

2. Geologic setting

The Qinling orogen is tectonically situated between the North China Craton and the South China Block (Fig. 1). It is connected with the Qilian and Kunlun orogens to the west, and the Dabie-Sulu orogen to the east (inset of Fig. 1). The Qinling orogen consists of the North Qinling and South Qinling belts that are separated by the late Paleozoic Shangdan suture zone (Meng and Zhang, 2000; Zhang et al., 2001). The South Qinling belt is bounded on the south by the Songpan-Ganze terrane, which is separated from the South China Block by the Triassic Animaque-Mianlue suture (inset of Fig. 1; Dong et al., 2011 and references therein).

The Qinling orogen was generated by two episodes of subduction and collision in Ordovician to Devonian and Permian to Late Triassic time, respectively (Kröner et al., 1993; Zhang et al., 2004, 2001). The North Qinling belt was produced by northward subduction of the Shangdan ocean, which was a branch of the proto-Tethyan ocean, and subsequent arc-continent collision between the North Qinling Terrane and North China Craton after closure of the Er'langping back-arc basin in the middle Devonian (Kröner et al., 1993). Contemporaneous rifting and subsequent southward drifting of the South China block formed the Mianlue ocean (Paleo-Tethyan ocean), which separated the South Qinling Terrane from the northern margin of the South China Block during Devonian to Permian time (Meng and Zhang, 2000). The Qinling orogen formed in the Triassic by diachronous collision between the South China Block and the South Qinling terrane along the Mianlue Suture zone (Jiang et al., 2010; Meng and Zhang, 2000; Zhang et al., 2004).

The Qinling orogen is traditionally divided into the East Qinling and the West Qinling, with the boundary roughly along the Baoji-Chengdu Railway (Zhang et al., 1996). The West Qinling orogen is bounded by the Linxia-Wushan-Tianshui Fault (Shangdan suture) on the north and the Animaque-Mianlue suture on the south, and extends westward to the East Kunlun orogen and Qaidam terrane (Fig. 1; Feng et al., 2002). Stratigraphically, the West Qinling orogen is dominated by early Paleozoic to Triassic marine sedimentary rocks that were pervasively folded and faulted during Triassic orogenic deformation (Meng and

Zhang, 2000). The Paleozoic strata variably experienced pumpellyite to greenschist facies metamorphism, whereas the Triassic rocks are typically unmetamorphosed (Dong et al., 2011). Mesozoic and Cenozoic terrestrial sediments are present in intermontane basins or foreland basins.

Granitoid intrusions are widespread throughout the West Qinling orogen. The rocks are metaluminous to peraluminous, moderate to high-K calc-alkaline, and enriched in LILE and LREE but depleted in HFSE, Nb, and Ta (Dong et al., 2011; Zhang et al., 2008). Zircon U-Pb dates show that these granitoid intrusions were emplaced in the 245–200 Ma interval during and after formation of the Animaque-Mianlue suture (Dong et al., 2011; Zhang et al., 2008). Regionally, the intrusions become older from east (~225–200 Ma; Qin et al., 2009; Sun et al., 2002) to west (245–233 Ma; Jin et al., 2005; Li et al., 2015b; Luo et al., 2015, 2012; Xu et al., 2014). The Triassic granitoid intrusions in the eastern segment of the West Qinling orogen are thought to have formed in a syn-collisional to post-collisional setting coupled with thickening and delamination of orogenic crust (Zhang et al., 2008) or breakoff of the subducted oceanic plate (Sun et al., 2002). The early to middle Triassic granitoids in the western segment of the West Qinling orogen are variably associated with mafic-ultramafic intrusions and andesitic to rhyolitic volcanic rocks, which have geochemical and isotopic signatures indicative of a subduction-related arc magmas (Guo et al., 2012; Li et al., 2014b).

3. Geology of the Xiahe-Hezuo district

The Xiahe-Hezuo district in the western segment of the West Qinling orogen is divided into eastern and western zones by the Xiahe-Lintan fault, which are stratigraphically dominated by uplifted Carboniferous to Permian sequences and down dropped Triassic strata, respectively (Fig. 2). The lower Carboniferous Badu Formation (Fm.) and upper Carboniferous Xiajialing Fm. consist of sandstone, siltstone, thin- to thick-bedded limestones and clastic limestones. The Permian Maomaolong Fm. is divided into lower and upper members. The lower member constitutes a complete Bouma sequence that changes from thick calcirudite and conglomerate at the bottom to sandstone, siltstone and mudstone at the top, and is indicative a continental slope environment (Wang et al., 1995; Zhao and Yang, 1992). The upper member consists of laminated carbonaceous silty mudstones and minor fine-grained calcareous sandstone that exhibit turbidite structures such as graded bedding, current ripple marks, and alternating sequences. Carbonaceous mudstone in the upper member contains abundant fine-grained pyrite that is considered to be diagenetic in origin (Yin et al., 1992; Zhao and Yang, 1992). The Triassic sequence in the western zone consists of the lower Triassic Shangaling Fm. and middle Triassic Gulangdi Fm. The Shangaling Fm. is dominated by deep sea basinal facies siltstones, calcareous siltstones and mudstones, with minor amounts of siliceous nodules in a few siltstone layers. The Gulangdi Fm. consists of interbedded sandstones, siltstones, calcareous siltstones, and mudstones.

Triassic orogenic deformation has generated a number of NW-striking folds and thrust faults, as best illustrated by the Xinpu-Lishishan anticline and the Xiahe-Lintan fault (Fig. 2). The Xinpu-Lishishan anticline consists of Carboniferous carbonates and siltstones in the core and Permian and Triassic clastic and carbonate rocks on both flanks (Fig. 2). Several reverse faults formed in association with the Xinpu-Lishishan anticline. The Xiahe-Lintan fault, which is the western segment of the > 400-km-long Xiahe-Lintan-Liangdang regional thrust system (Zhang et al., 2001), is the most prominent fault structure in this district (Fig. 2). It extends along an approximately NWW strike and dips 50°–70° to north, with a surface trace of more than 60 km. The Xiahe-Lintan fault separates the Triassic flysch in the west from the late Paleozoic sequence in the east. Secondary or higher order faults, broadly parallel to the Xiahe-Lintan fault, are well developed in the western zone of the district (Fig. 2). These secondary structures,

particularly their intersections, have been important in localizing gold mineralization.

Mesozoic igneous rocks are widespread in the Xiahe-Hezuo district (Fig. 2). Several granitoid plutons intrude Permian sedimentary rocks in the uplifted eastern zone whereas numerous small stocks and dikes intrude the Triassic sequence in the down dropped western zone. The Meiwu, Dewulu, Daerzang, and Ayishan plutons consist of quartz diorite, granodiorite, and granite. Laser ablation ICP-MS and SHRIMP zircon U-Pb dates indicate that these granitoid intrusions were emplaced between 248 and 233 Ma (Jin et al., 2005; Luo et al., 2015; Xu et al., 2014). The high Mg numbers (50–58) of the granitoid intrusions and abundance of mafic microgranular enclaves therein indicate that mixing of mafic mantle-derived melt and felsic crustal-derived melt was involved in their petrogenesis (Luo et al., 2015). The stocks and dikes in the western zone have diorite, quartz diorite, granodiorite, and granite compositions that are similar to plutonic bodies in the eastern zone. Volcanic rocks composed of andesite and dacite outcrop adjacent to the Dewulu quartz diorite pluton (Fig. 2), and have a zircon U-Pb date of 239 ± 2 Ma(MSWD = 2; Luo, 2013). The geochemical and Sr-Nd-Hf isotopic compositions of Triassic volcanic rocks suggest they formed via fractional crystallization of a metaluminous calc-alkaline andesitic melt that assimilated pelitic rocks (Luo, 2013). A small volume of Cretaceous potassic tholeiitic basalts with an intracontinental oceanic island basalt (OIB) signature is exposed in the northern and northwestern parts of the district (Huang et al., 2013a).

4. Geology of the Zaozigou gold deposit

The Zaozigou gold deposit (34°57′–34°59′ N, 102°47′–102°47′ E) in the western zone of the Xiahe-Hezuo district is located about 11 km southwest of the city of Hezuo (Fig. 2). The geology of the mining area is dominated by the middle Triassic Gulangdi Fm. consisting of carbonaceous argillaceous to siliceous siltstones and mudstones with minor amounts of greywacke and limestone (Liu et al., 2011). These sedimentary rocks are intruded by numerous intermediate to felsic dikes (Fig. 3). Granodiorite dikes are predominant in the eastern part of the mining camp. They intrude along bedding parallel fractures (Fig. 4A), northeast-striking fractures and, less commonly, northwest striking fractures. These dikes contain up to 35 vol% coarse-grained plagioclase phenocrysts (1–4 mm in diameter), lesser medium-grained biotite (7–10 vol%), hornblende (< 5 vol%) and rare resorbed quartz phenocrysts (Fig. 4B). The groundmass includes fine- to medium-grained

intergrowths of K-feldspar, plagioclase, quartz and biotite. Porphyritic quartz diorite dikes are common in the western half of the mining area and some of them crosscut the granodiorite dikes (Figs. 3 and 4C). Phenocrysts in quartz diorite are dominated by medium-grained plagioclase (10–12 vol%) with minor biotite, hornblende and garnet (Fig. 4D). The groundmass contains the same assemblage but has more quartz (15 vol%), less hornblende and lacks garnet. Diorite porphyry dikes are scattered across the mining area, but are common in the western part of the mine. The diorite porphyry dikes (Fig. 4E and F) contain abundant phenocrysts of plagioclase, biotite and minor hornblende dispersed in a groundmass consisting of fine-grained phenocryst minerals. Accessory minerals in each dike type are broadly consistent and include zircon, apatite, titanite and ilmenite. The absence of magnetite and abundance of ilmenite are indicative of the reduced nature of these magmas. Hydrothermally altered and gold mineralized granodiorite and porphyritic quartz diorite dikes (Fig. 4C) are commonly cut by fresh diorite porphyry dikes (Fig. 4F); the latter are locally displaced by NS-striking stibnite-quartz veins (Fig. 3).

There are numerous higher-order faults in the mining area (Fig. 3) with northeast, roughly south-north and northwest orientations (Wei et al., 2018). NE-striking faults are the most important ore-hosting structures in the east part of mining area. The NE-striking faults are commonly 1000–3000 m long, 0.5–10 m wide, and strike from 40° to 60° with dip angles generally greater than 70° to the northwest or, less commonly, to the southeast. The western edge of the Zaozigou mining area is marked by a group of NS-striking normal faults (Fig. 3), which are 400 to > 1000 m long, < 1 to 22 m wide and commonly dip 60°–70° east or west. There are also a number of NW-striking gently-dipping faults, which intersect and offset the above mentioned faults. These faults are commonly several hundred meters long, and range in strike from 260° to 245° with dip angles of 8–32°. The NW-striking faults and some NS-striking gold ore bodies are locally filled with stibnite-quartz veins. The sediment-hosted gold ores and Sb-(Au) veins are related to different stages of deformation (Wei et al., 2018). The first stage (D₁) is characterized by NE-striking sinistral transtensional normal shearing and NS-striking dextral transpressional thrusts and is considered to be synchronous with gold mineralization. This stage is followed by sinistral transtensional reactivation along the NS-striking faults, with development of dextral, NW-trending, gently-dipping faults (D₂). Dilational zones of NS- and NW-striking faults facilitated emplacement of younger auriferous stibnite-quartz veins.
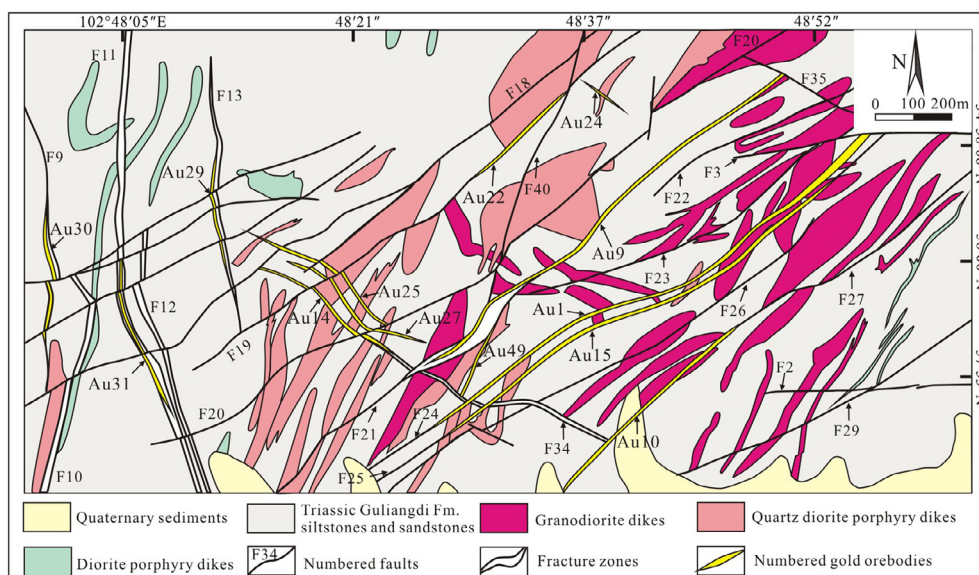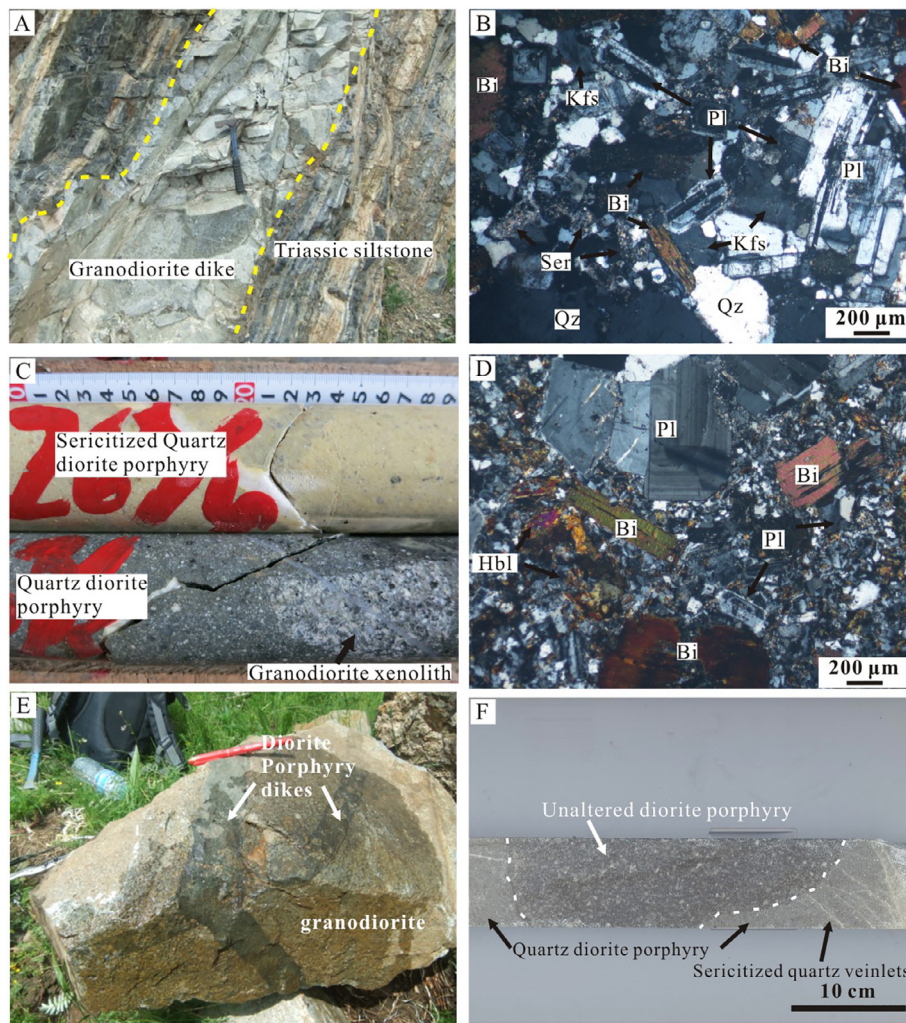

Fig. 3. Geologic map of the Zaozigou gold deposit (after Liu et al., 2011).

Fig. 4. Photographs showing morphology, cross-cutting relationships and mineralogy of the igneous dikes. A. Granodiorite dike intruding the Triassic siltstones along stratification. B. Photomicrograph showing the mineralogy and texture of a granodiorite dike (cross-polarized light). C. Quartz diorite porphyry dike revealed by drill hole in the mine. Note the lower fresh quartz diorite porphyry contains a granodiorite xenolith, the upper one is intensively sericitized quartz diorite porphyry with disseminated pyrite and arsenopyrite, D. Photomicrograph showing the mineralogy and texture of a quartz diorite porphyry dike (cross-polarized light). E. Two diorite porphyry dikes intruding granodiorite. The diorite porphyry dike containing numerous inclusions of granodiorite is crosscut by an inclusion-free diorite porphyry dike, indicating multiple injections of dioritic magma. F. Drill hole showing fresh diorite porphyry dike intruding an altered quartz diorite porphyry dike. Note sericitized quartz veinlets in quartz diorite are crosscut by the diorite dike. Abbreviations: Bi = biotite, Hbl = hornblende, Kfs = K-feldspar, Pl = plagioclase, Qz = quartz, Ser = sericite.

5. Mineralization and alteration

5.1. Gold orebodies

The Zaozigou gold deposit was discovered in 1996 as a small prospect; exploration continued until the end of 2012 with proven reserves of 142 t at an average grade of 2.69 g/t (Chen et al., 2011, 2015). The deposit consists of 104 orebodies, but about 80% of gold reserves are contained in ten major orebodies, including Au1, Au9, Au10, Au14, Au15, Au25, Au29, Au31, Au46, and M6 (Figs. 3 and 5). Mineralization is controlled predominantly by NE-trending high-angle normal faults, as expressed by the most important orebodies Au1, Au9, Au10, Au15, and Au46. The NS-trending faults also host some economically important orebodies, such as Au29, Au31. Of these, Au1 is the largest orebody, containing 23.8 t gold at an average grade of 4.6 g/t. It is 1160 m long and 1–17 m thick, with a minimum vertical extent of 1030 m from 3250 to 2220 m above sea level (Chen et al., 2015). This orebody is localized in the high-angle (82–87°) F24 fault and is offset by the gently dipping M6 Sb-(Au) orebody at about 3120 m elevation (Fig. 5). The gently dipping faults also accommodate other Sb-(Au) orebodies, such as M3, M4, and M10, in other parts of the mine. Many steeply dipping gold orebodies are exposed at the surface and the upper portions were variably oxidized and partly eroded. However, most of the gently dipping Sb-(Au) veins were not unexposed.

5.2. Mineralization

The main stage of gold mineralization at Zaozigou consists of disseminated fine-grained pyrite and arsenopyrite in hydrothermally altered clastic rocks of the middle Triassic Gulangdi Fm. (Fig. 6A and C) and, less importantly, in NE- and NS-trending porphyritic quartz-diorite to granodiorite dikes (Fig. 6B and D). Both sediment- and dike-hosted ores have gold grades ranging from 0.1 to 25 g/t, but up to 224 g/t (Chen et al., 2015). Fine-grained pyrite and arsenopyrite are the predominant auriferous minerals (Fig. 7A and B) and locally occur with trace amounts of sphalerite and chalcopyrite. Pyrite is generally subhedral to anhedral, cubic or pyritohedron in form, but locally forms aggregates a few millimeters across. Arsenopyrite is generally prismatic or forms sub-micron to 3 mm long needles. In dike-hosted ores, pyrite-arsenopyrite aggregates commonly replace biotite and hornblende (Fig. 7B). Such gold mineralization is generally accompanied by gold-bearing sulfide-quartz-ankerite veinlets, typically 0.5–5 mm in thickness (Figs. 6E and 7C). Such veinlets are universal in the steeply-dipping NE-striking orebodies, but are rare in the NS-striking varieties. Fine-grained pyrite and arsenopyrite aggregates account for 3–20 vol% of individual veinlets and are associated with minor to trace amounts of chalcopyrite, tetrahedrite, sphalerite and scheelite. In places, native gold (2–30 μm) grains occur as microfracture infillings in pyrite or interstitial to pyrite, arsenopyrite and ankerite grains (Cao et al., 2012; Liu et al., 2011).

Stibnite-quartz veins or stockworks overprint the sediment-hosted gold ores and locally offset the steeply-dipping gold orebodies. In the
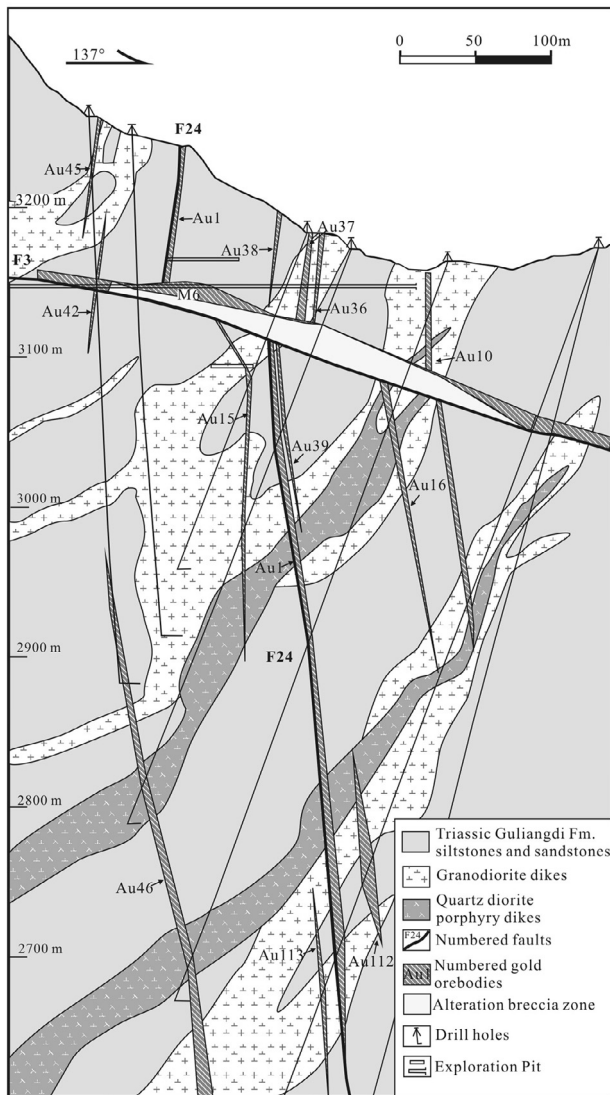
Fig. 5. Representative exploration cross section showing the occurrence and morphology of orebodies in the Zaozigou gold deposit (after Sui, 2016).

western part of mining area, the subvertical NS-striking orebodies are locally brecciated and cemented by stibnite-quartz veins. Most stibnite-quartz veins are several to a few tens of centimeters in thickness, but range up to 2 m in the gently dipping M6 orebody (Figs. 5 and 6F). The veins are dominated by quartz and stibnite (5–30 vol%), with minor ankerite (Fig. 7D). Gold grades vary from 0.02 to 4 g/t in the quartz-stibnite veins (Liu et al., 2011). Gold grains, 2–30 μm in diameter, are locally seen as inclusions in quartz and stibnite.

5.3. Alteration

Ore-related alteration at Zaozigou consists of sericitization, chloritization, silicification and carbonatization. Sericitization is intimately associated with disseminated pyrite and arsenopyrite in high grade gold ores. Sericite, quartz and ankerite typically replace feldspars both in sedimentary rocks and igneous dikes (Fig. 6C and D). Chloritization is best developed in sedimentary rocks peripheral to sericitized zones. Although disseminated pyrite and arsenopyrite are also present in chloritized siltstones, gold contents are generally less than 0.3 g/t gold.

6. Samples and analytical methods

6.1. $^{40}Ar/^{39}Ar$ dating of ore-related hydrothermal sericite

$^{40}Ar/^{39}Ar$ dating was performed on sericite separates from dike-hosted ore (sample ZG30) and siltstone-hosted ore (sample ZG47), which were taken from underground workings of the Au9 and Au1 orebodies, respectively. The samples were crushed in a mortar and pestle, the 0.25–0.5 mm size fraction was washed in distilled water in an ultrasonic bath for 1 h, and dried. Pure sericite aggregates were obtained by hand-picking under a binocular microscope. The mineral separates were loaded into an irradiation disk along with Fish Canyon sanidine standard (28.201 ± 0.046; Kuiper et al., 2008). The disk was wrapped in Al-foil, vacuum-sealed in silica glass tubes, and then irradiated for 14 h in the Cadmium-lined B-1 CLICIT facility at the Radiation Center, Oregon State University, USA. The standard mineral Fish Canyon sanidine was used to calculate the irradiation parameter (J). Sample and flux monitor irradiation geometry followed those of Vasconcelos et al. (2002). After a decay period, samples were step heated using a CO_2 laser and argon isotopes analysed using a MAP215-50 mass spectrometer at the Argon Geochronology Laboratory, School of Earth Science, The University of Queensland, Australia. The analytical procedures used are described in detail by Vasconcelos et al. (2002) and are briefly summarized here. The minerals were heated incrementally with a continuous-wave Verdi Diode laser (532 nm). The fraction of gas released was cleaned through a cold-trap (T = −125 °C) and two C-50 SAES Zr-V-Fe getters. Full system blanks and air pipettes were determined before and after each sample. The data were corrected using the software "MassSpec Version 7.527" developed by Alan Deino of the Berkeley Geochronology Centre, USA (Deino and Potts, 1990). All dates are reported using $5.543 \times 10^{-10} a^{-1}$ as the total decay constant for ^{40}K (Steiger and Jäger, 1977), and the values for the reactor correction factors are $(7.04 \pm 0.06) \times 10^{-4}$ for $(^{39}Ar/^{37}Ar)_{Ca}$, $(2.64 \pm 0.02) \times 10^{-4}$ for $(^{36}Ar/^{37}Ar)_{Ca}$, and $(8 \pm 3) \times 10^{-3}$ for $(^{40}Ar/^{39}Ar)_K$. A $^{40}Ar/^{36}Ar$ value of 298.56 ± 0.31 for atmospheric argon was used for the calculation of the mass spectrometer discrimination (Renne et al., 2009). All $^{40}Ar/^{39}Ar$ dates are reported with 2 sigma errors.

6.2. Laser ablation ICP-MS zircon U-Pb dating

Six dike samples were obtained from underground workings, drill cores and outcrops. Sample ZZG27 is an altered and mineralized granodiorite dike taken from the NE-striking Au9 orebody on the 3150 m level. Sample ZA39 was collected from an altered and mineralized porphyritic quartz diorite on the 3150 m level, which was cut by the NE-striking Au1 orebody. Sample 16-ZG306 is a fresh diorite porphyry dike at 279–280 m depth of drill hole ZK8524 that crosscuts a sericitized porphyritic quartz diorite dike in the vicinity of the steeply-dipping, NE-striking, Au15 orebody (Fig. 4F). Sample 12-ZG42 is from an outcrop of a NNE-trending diorite porphyry dike that crosscuts a barren NE-trending granodiorite dike in the eastern part of mining area. Samples 12-ZG44 and 12-ZG45 are from two NS-trending diorite porphyry dikes in the western part of the mining area that are crosscut and sericitized by NS-trending quartz-stibnite veins (Fig. 3).

100–200 zircon crystals from each sample were hand-picked under a binocular microscope, and then mounted in an epoxy resin. The resin was polished to expose the interior of the crystals. Transmitted- and reflected-light photographs and cathodoluminescence (CL) images were used to characterize the internal textures of zircon grains. Laser ablation ICP-MS U-Pb dating was conducted using an Agilent 7500a ICP-MS instrument equipped with a GeoLas2005 193 nm ArF excimer laser at the State Key Laboratory of Geological Processes and Mineral Resources, China University of Geosciences, Wuhan. Detailed operating conditions for the laser ablation system and the ICP-MS instrument and data reduction follow those in Liu et al. (2008). A beam diameter of
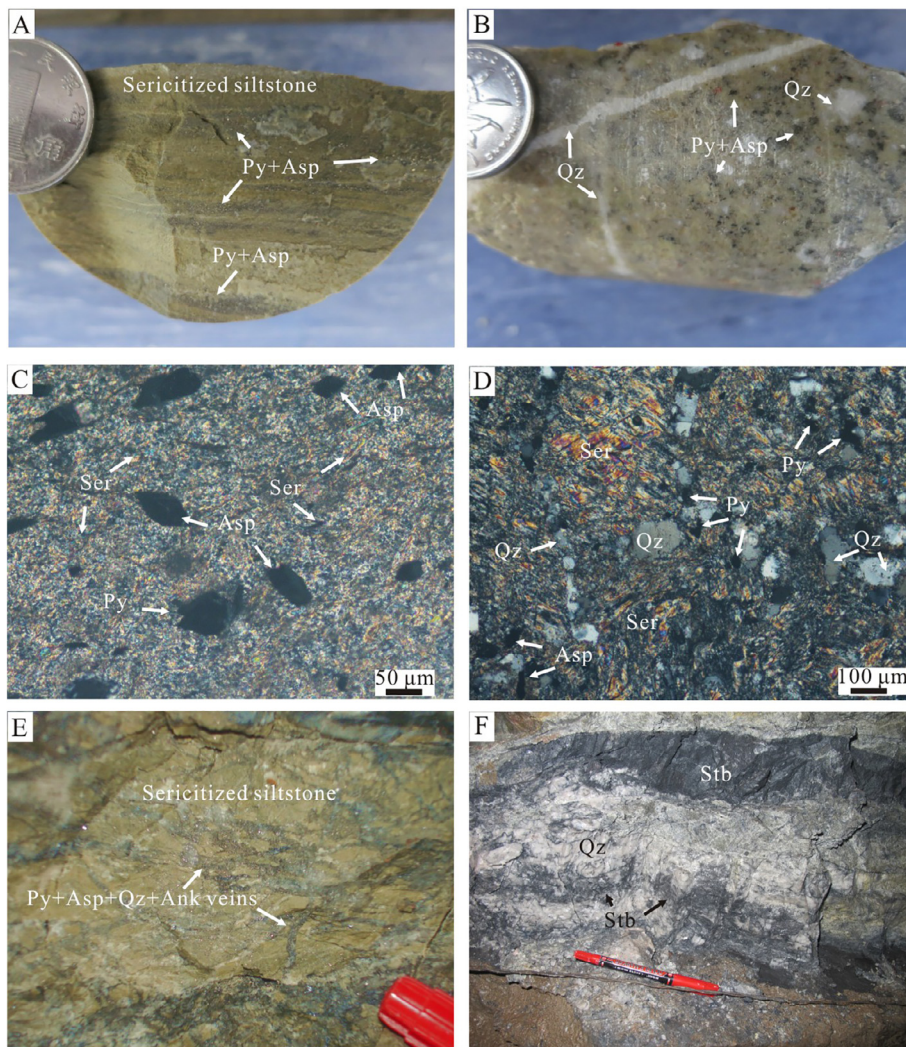
Fig. 6. Photographs showing the textures of gold ores and alteration. A. Disseminations of pyrite and arsenopyrite in sericitized siltstone. B. Disseminated pyrite and arsenopyrite replacing biotite and hornblende in sericitized granodiorite. C. Transmitted light photomicrograph of sediment-hosted disseminated ore with pyrite and arsenopyrite in sericitized siltstone. Detrital aluminosilicate minerals in siltstone were replaced by sericite and quartz. D. Transmitted light photomicrograph of dike-hosted disseminated ore showing feldspars completely replaced by sericite and quartz. E. Sericitic siltstone with disseminated pyrite and arsenopyrite overprinted by quartz-ankerite veinlets containing aggregates of fine-grained pyrite and arsenopyrite. F. Stibnite – quartz vein. Abbreviations: Ank = ankerite, Asp = arsenopyrite, Py = pyrite, Qz = quartz, Ser = sericite, Stb = stibnite.
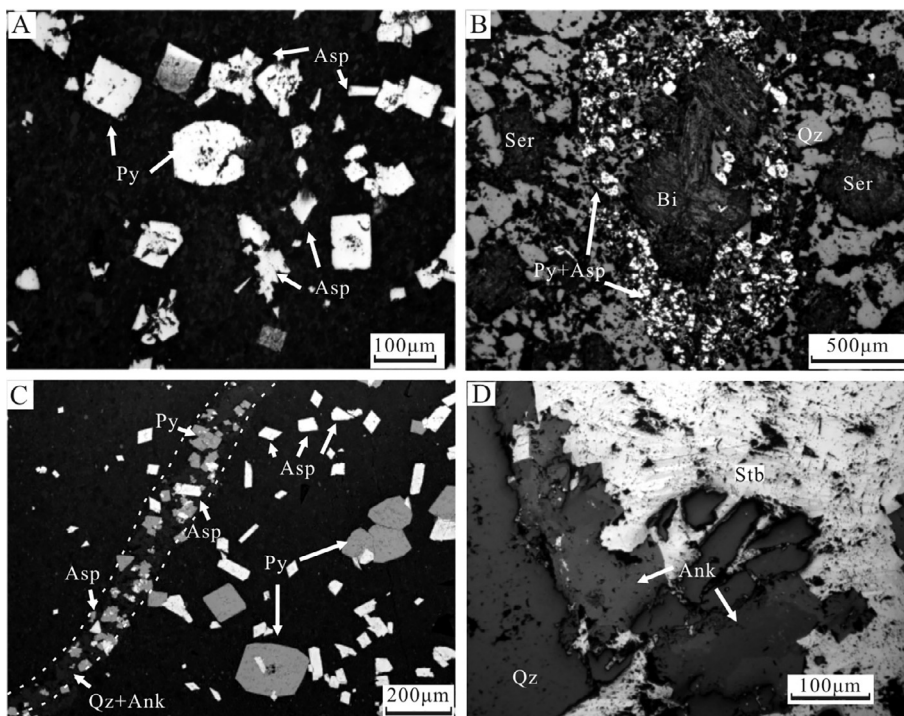
Fig. 7. Reflected-light photomicrographs and backscattered electron images showing ore mineralogy and textures of the Zaozigou gold deposit. A. Disseminated pyrite and arsenopyrite in sericitized siltstone. B. Replacement of biotite in sericitized granodiorite-hosted ore by pyrite-arsenopyrite aggregates. C. Pyrite (Py2)-arsenopyrite (Asp2) bearing quartz-ankerite veinlet cutting sericitized siltstone-hosted disseminations of pyrite (Py1) and arsenopyrite (Asp1) (backscattered electron image). D. Stibnite and ankerite filling fractures in quartz vein. Abbreviations as in Fig. 6.

Table 1
$^{40}Ar/^{39}Ar$ Data of Hydrothermal Sericite from the Zaozigou Gold Deposit.

Run ID	$^{40}Ar/^{39}Ar$	$^{36}Ar/^{39}Ar$	$^{37}Ar/^{39}Ar$	$^{38}Ar/^{39}Ar$	$^{40}Ar^*/^{39}Ar$	$^{40}Ar^*$(%)	Apparent age (Ma)	± 1σ (Ma)	^{39}Ar Moles	^{40}Ar Moles	^{40}Ar Disc	± 1σ
Sample ZG30, J value = 0.003708 ± 0.000005												
9001-01A	39.697	0.001	0.336	0.012	39.377	99.17	245.87	0.47	4.0E−14	1.60E−12	1.0028	0.0009
9001-01B	39.101	0.000	0.248	0.012	39.082	99.93	244.15	1.13	9.6E−15	3.75E−13	1.0028	0.0009
9001-01C	39.242	0.000	0.324	0.013	39.316	100.17	245.52	1.53	5.6E−15	2.20E−13	1.0028	0.0009
9001-01D	39.899	0.003	0.182	0.012	39.165	98.15	244.63	1.42	4.7E−15	1.89E−13	1.0028	0.0009
9001-01E	39.260	0.001	0.535	0.013	38.993	99.29	243.63	1.45	4.3E−15	1.67E−13	1.0028	0.0009
9001-01F	40.199	0.002	0.053	0.013	39.685	98.72	247.67	2.17	3.0E−15	1.20E−13	1.0028	0.0009
9001-01G	40.340	0.002	0.651	0.012	39.780	98.57	248.22	1.55	3.7E−15	1.48E−13	1.0028	0.0009
9001-01H	40.176	0.003	0.238	0.013	39.306	97.82	245.46	3.93	1.6E−15	6.39E−14	1.0028	0.0009
9001-01I	99.647	0.067	5.006	0.035	80.437	80.44	470.91	79.31	8.4E−17	8.37E−15	1.0028	0.0009
9001-01J	−13.515	−0.024	6.008	−0.035	−5.967	43.96	−40.36	57.10	−8.2E−17	1.10E−15	1.0028	0.0009
Sample ZG47, J value = 0.003708 ± 0.000005												
9004-02A	46.707	0.029	−0.371	0.018	37.968	81.31	237.63	5.68	8.85E−16	4.13E−14	1.0026	0.0009
9004-02B	41.534	0.006	−0.274	0.013	39.636	95.45	247.38	2.30	2.34E−15	9.72E−14	1.0026	0.0009
9004-02C	39.432	0.002	0.260	0.012	38.863	98.54	242.87	0.88	1.00E−14	3.95E−13	1.0026	0.0009
9004-02D	39.247	0.002	1.108	0.012	38.695	98.52	241.89	0.94	9.29E−15	3.65E−13	1.0026	0.0009
9004-02E	39.527	0.003	2.249	0.012	38.798	98.00	242.49	0.70	1.73E−14	6.83E−13	1.0026	0.0009
9004-02F	39.031	0.002	0.228	0.012	38.455	98.51	240.48	0.63	1.76E−14	6.89E−13	1.0026	0.0009
9004-02G	39.431	0.002	0.027	0.011	38.889	98.63	243.02	0.99	1.08E−14	4.25E−13	1.0026	0.0009
9004-02H	40.091	0.004	0.049	0.013	38.968	97.20	243.48	1.03	7.10E−15	2.85E−13	1.0026	0.0009
9004-02I	47.198	0.025	0.857	0.022	39.890	84.47	248.86	10.05	4.92E−16	2.32E−14	1.0026	0.0009
9004-02J	69.542	0.130	−25.062	0.111	28.230	41.30	179.60	103.96	3.60E−17	2.51E−15	1.0026	0.0009

$^{40}Ar^*$ = radiogenic ^{40}Ar.

32 mm was used. Zircon 91500 was used as external standard for U-Pb dating and was analyzed twice every 5 analyses. Off-line selection and integration of background and analytical signals, time-drift corrections, and U-Pb isotope ratios were calculated using in-house software called ICPMSDataCal (Liu et al., 2008). Concordia diagrams and weighted mean age calculations were made using Isoplot (Ludwig, 2003). All U-Pb dates are reported with 2 sigma errors

7. Results

7.1. Sericite $^{40}Ar/^{39}Ar$ ages

$^{40}Ar/^{39}Ar$ isotope data on sericite from two samples (ZG30 and ZG47) are summarized in Table 1 and the age spectra are depicted in Fig. 8. Both samples yield well-defined age plateaus consisting of more than 90% of the total ^{39}Ar released. Sericite aggregates from sample ZG30 give an $^{40}Ar/^{39}Ar$ plateau age of 245.6 ± 1.0 Ma (MSWD = 1.2; Fig. 8A) and an integrated age of 246.2 ± 1.2 Ma. Sericite from sample ZG47 has a slightly younger plateau age of 242.1 ± 1.2 Ma (MSWD = 1.6; Fig. 8B) and an integrated age of 242.3 ± 1.0 Ma. The perfectly flat spectra accounting for > 95% ^{39}Ar released suggest that there is only one generation of sericite in each sample. Furthermore, the consistency between the plateau age and integrated age of individual samples preclude the presence of excess argon in the mineral and any argon loss since the mineral cooled below the closure temperature of argon isotopes in mica. Thus, the $^{40}Ar/^{39}Ar$ plateau ages are interpreted to be the best estimates of the age of sericitic alteration and associated gold mineralization.

7.2. Zircon U-Pb ages

Zircon U-Pb isotope data of the six dike samples are summarized in Table 2 and graphically illustrated in Concordia diagrams (Fig. 9). Zircons from all samples are consistently transparent, colorless to pale brown, and prismatic in morphology. Zircon grains from the granodiorite (sample ZZG27) are 80–300 μm across, with length/width ratios of 2:1–3:1. Quartz diorite porphyry and diorite porphyry samples have smaller zircons (30–150 μm in diameter) with higher aspect ratios (up to 5:1). In cathodoluminescence images, most zircon grains from granodiorite and quartz diorite porphyry show spectacular oscillatory
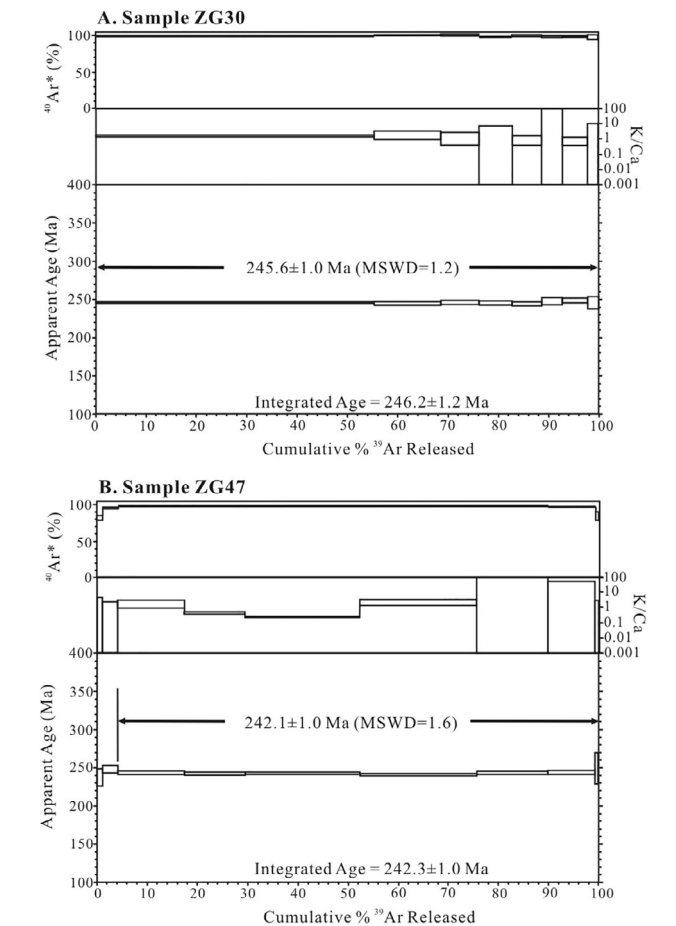
Fig. 8. $^{40}Ar/^{39}Ar$ age spectra of ore-related sericite from sericitized granodiorite-hosted (A) and siltstone-hosted (B) ores in the Zaozigou gold deposit.

concentric zoning. A few grains exhibit core-rim structures, indicating the existence of inherited zircons (Corfu et al., 2003). Zircons from the diorite porphyry (sample 16-ZG306; 12-ZG44 and 12-ZG45) are characterized by broad growth zoning in CL images, with minor oscillatory

Table 2
LA-ICP-MS Zircon U-Pb Data of Intermediate to Felsic Dikes from the Zaozigou Gold Deposit.

Spot	Th/U	Isotope ratio						Age (Ma)					
		$^{207}Pb/^{206}Pb$	± 1σ	$^{207}Pb/^{235}U$	± 1σ	$^{206}Pb/^{238}U$	± 1σ	$^{207}Pb/^{206}Pb$	± 1σ	$^{207}Pb/^{235}U$	± 1σ	$^{206}Pb/^{238}U$	± 1σ
Sample ZZG27, granodiorite dike													
ZZG27-01	0.04	0.0521	0.0016	0.2822	0.0087	0.0392	0.0004	300.4	73.3	252.6	7.2	248.9	2.3
ZZG27-02	0.16	0.0521	0.0017	0.2825	0.0091	0.0395	0.0004	287.2	74.7	253.5	7.7	249.2	3.4
ZZG27-03	0.09	0.0669	0.0012	1.0982	0.0515	0.1166	0.0049	835.4	37.3	752.3	25.6	711.1	28.2
ZZG27-04	0.23	0.0525	0.0019	0.2823	0.0102	0.039	0.0004	309.4	79.6	252.3	8.1	247.0	3.6
ZZG27-05	0.05	0.0513	0.0012	0.2768	0.0064	0.0391	0.0004	254.4	56.8	248.3	5.1	247.0	3.6
ZZG27-06	0.13	0.0505	0.0013	0.301	0.008	0.043	0.0004	220.0	56.0	267.0	6.0	272.0	3.0
ZZG27-07	0.09	0.0509	0.0011	0.2805	0.0065	0.0398	0.0004	235.5	48.4	251.3	5.4	252.2	3.1
ZZG27-09	0.07	0.051	0.0013	0.2804	0.0075	0.0397	0.0004	243.0	56.0	251.0	6.0	251.0	2.0
ZZG27-10	0.14	0.0537	0.002	0.2894	0.0099	0.0394	0.0005	367.3	83.6	258.5	8.6	249.5	3.2
ZZG27-11	0.07	0.0523	0.0015	0.3096	0.0085	0.0429	0.0005	298.9	65.3	274.8	7.1	271.4	3.4
ZZG27-12	0.09	0.0539	0.0012	0.2948	0.0066	0.0395	0.0003	369.1	50.8	262.1	5.1	250.3	2.8
ZZG27-13	0.1	0.0537	0.0014	0.2901	0.0078	0.0391	0.0004	367.2	61.0	259.5	6.3	247.0	2.6
ZZG27-14	0.07	0.053	0.0009	0.2903	0.005	0.0396	0.0004	328.0	32.0	259.0	4.0	250.0	2.0
ZZG27-15	0.05	0.0524	0.0007	0.2853	0.0042	0.0393	0.0002	302.7	1.3	255.6	3.4	249.5	2.0
Sample ZA39, quartz diorite porphyry dike													
ZA39-1	0.09	0.0500	0.0015	0.2638	0.0083	0.0383	0.0004	194.5	72.2	237.7	6.6	242.3	2.3
ZA39-2	0.27	0.0486	0.0020	0.2563	0.0104	0.0382	0.0004	131.6	100.9	231.7	8.4	241.9	2.6
ZA39-3	0.21	0.0508	0.0022	0.2685	0.0111	0.0386	0.0004	231.6	98.1	241.5	8.9	244.0	2.7
ZA39-4	0.15	0.0496	0.0020	0.2564	0.0105	0.0376	0.0005	176.0	126.8	231.7	8.5	237.7	3.0
ZA39-5	0.19	0.0538	0.0020	0.2910	0.0102	0.0395	0.0004	364.9	81.5	259.4	8.0	249.5	2.6
ZA39-7	0.05	0.0514	0.0012	0.2748	0.0069	0.0389	0.0006	257.5	51.8	246.5	5.5	246.2	3.8
ZA39-9	0.06	0.0514	0.0013	0.2730	0.0071	0.0388	0.0006	261.2	52.8	245.1	5.7	245.7	3.8
ZA39-10	0.05	0.0512	0.0012	0.2718	0.0065	0.0388	0.0003	250.1	55.5	244.2	5.2	245.3	2.1
ZA39-11	0.27	0.0514	0.0015	0.2717	0.0078	0.0390	0.0005	257.5	66.7	244.0	6.3	246.4	3.2
ZA39-14	0.25	0.0528	0.0016	0.2810	0.0081	0.0389	0.0004	320.4	66.7	251.4	6.4	246.3	2.3
ZA39-15	0.07	0.0513	0.0018	0.2741	0.0098	0.0390	0.0004	253.8	88.0	246.0	7.8	246.6	2.6
ZA39-16	0.17	0.0510	0.0017	0.2695	0.0090	0.0384	0.0004	239.0	80.5	242.3	7.2	243.0	2.4
ZA39-17	0.03	0.0504	0.0011	0.2700	0.0057	0.0389	0.0004	213.0	48.1	242.7	4.5	245.9	2.3
ZA39-18	0.10	0.0520	0.0011	0.2798	0.0058	0.0390	0.0004	287.1	54.6	250.5	4.6	246.9	2.5
Sample 16-ZG306, quartz diorite porphyry dike													
16-ZG306-01	1.06	0.0511	0.0012	0.2689	0.0065	0.0378	0.0004	255.6	55.5	241.8	5.2	238.9	2.3
16-ZG306-02	1.27	0.0516	0.0013	0.2728	0.0067	0.0379	0.0004	333.4	57.4	245.0	5.3	239.7	2.4
16-ZG306-03	1.25	0.0504	0.0014	0.2786	0.0075	0.0396	0.0004	213.0	64.8	249.6	5.9	250.5	2.3
16-ZG306-04	0.97	0.0537	0.0019	0.2838	0.0116	0.0376	0.0005	366.7	81.5	253.7	9.2	237.7	2.9
16-ZG306-05	1.18	0.0506	0.0013	0.2655	0.0068	0.0377	0.0003	220.4	59.2	239.1	5.5	238.4	2.1
16-ZG306-06	1.30	0.0505	0.0011	0.2625	0.0061	0.0375	0.0003	216.7	84.2	236.7	4.9	237.2	1.9
16-ZG306-07	0.85	0.0495	0.0013	0.2564	0.0067	0.0373	0.0004	172.3	54.6	231.7	5.5	236.3	2.4
16-ZG306-08	0.84	0.0504	0.0013	0.2631	0.0070	0.0376	0.0004	213.0	89.8	237.2	5.7	237.9	2.4
16-ZG306-09	1.26	0.0500	0.0013	0.2608	0.0069	0.0376	0.0004	194.5	61.1	235.3	5.6	238.0	2.3
16-ZG306-10	1.20	0.0504	0.0012	0.2633	0.0064	0.0376	0.0004	216.7	83.3	237.3	5.1	237.8	2.4
16-ZG306-11	0.69	0.0496	0.0012	0.2547	0.0065	0.0369	0.0004	176.0	55.5	230.4	5.3	233.5	2.4
16-ZG306-12	1.27	0.0489	0.0012	0.2550	0.0061	0.0375	0.0003	142.7	55.6	230.7	4.9	237.3	2.0
16-ZG306-13	1.24	0.0492	0.0012	0.2633	0.0062	0.0385	0.0004	166.8	55.5	237.4	5.0	243.4	2.3
16-ZG306-14	1.16	0.0494	0.0011	0.2570	0.0058	0.0374	0.0004	168.6	50.0	232.2	4.7	236.9	2.3
16-ZG306-15	1.07	0.0499	0.0011	0.2618	0.0060	0.0378	0.0004	190.8	19.4	236.1	4.8	239.2	2.2
16-ZG306-16	0.87	0.0511	0.0014	0.2599	0.0066	0.0368	0.0003	255.6	61.1	234.6	5.4	233.0	1.9
Sample 12-ZG42, diorite porphyry dike													
12-ZG42-1	0.13	0.0504	0.0023	0.2793	0.0134	0.0398	0.0006	213.0	107.4	250.1	10.6	251.7	3.7
12-ZG42-2	0.07	0.0506	0.0014	0.2628	0.0073	0.0373	0.0004	233.4	60.2	236.9	5.8	236.2	2.6
12-ZG42-3	0.11	0.0510	0.0022	0.2639	0.0108	0.0374	0.0004	239.0	102.8	237.8	8.7	236.6	2.8
12-ZG42-4	0.03	0.0488	0.0012	0.2552	0.0066	0.0377	0.0003	200.1	59.3	230.8	5.3	238.5	2.2
12-ZG42-5	0.03	0.0502	0.0017	0.2586	0.0086	0.0373	0.0005	205.6	75.9	233.6	7.0	235.9	2.9
12-ZG42-6	0.12	0.0515	0.0027	0.2684	0.0141	0.0379	0.0005	264.9	94.4	241.4	11.3	239.9	3.3
12-ZG42-7	0.15	0.0504	0.0018	0.2572	0.0090	0.0370	0.0004	213.0	86.1	232.4	7.3	234.3	2.6
12-ZG42-8	0.04	0.0486	0.0013	0.2457	0.0066	0.0366	0.0003	127.9	63.0	223.0	5.4	231.4	2.1
12-ZG42-9	0.07	0.0558	0.0028	0.2777	0.0130	0.0369	0.0005	455.6	113.0	248.8	10.3	233.5	3.2
12-ZG42-10	0.03	0.0502	0.0013	0.2606	0.0068	0.0375	0.0004	211.2	59.2	235.1	5.5	237.2	2.5
12-ZG42-11	0.18	0.0511	0.0021	0.2622	0.0103	0.0373	0.0005	255.6	97.2	236.4	8.3	236.3	2.8
12-ZG42-12	0.20	0.0502	0.0021	0.2591	0.0106	0.0377	0.0005	211.2	98.1	233.9	8.5	238.6	3.1
12-ZG42-13	0.05	0.0516	0.0015	0.2636	0.0077	0.0370	0.0004	264.9	68.5	237.6	6.2	234.0	2.3
12-ZG42-14	0.22	0.0526	0.0028	0.2688	0.0141	0.0376	0.0006	322.3	122.2	241.7	11.3	238.0	3.6
12-ZG42-15	0.23	0.0507	0.0026	0.2602	0.0132	0.0372	0.0006	227.8	118.5	234.8	10.7	235.4	3.5
12-ZG42-16	0.09	0.0507	0.0024	0.2645	0.0127	0.0378	0.0005	227.8	111.1	238.3	10.2	239.2	3.4
12-ZG42-18	0.10	0.0493	0.0021	0.2573	0.0103	0.0380	0.0005	166.8	96.3	232.5	8.4	240.7	3.1
Sample 12-ZG44, diorite porphyry dike													
12-ZG44-1	0.15	0.0495	0.0023	0.2534	0.0115	0.0371	0.0005	172.3	109.2	229.3	9.3	235.0	2.9
12-ZG44-2	0.25	0.0518	0.0025	0.2776	0.0132	0.0391	0.0005	276.0	111.1	248.7	10.5	247.3	3.4
12-ZG44-3	0.26	0.0537	0.0025	0.2730	0.0119	0.0372	0.0005	366.7	103.7	245.1	9.5	235.6	2.9
12-ZG44-4	0.14	0.0516	0.0026	0.2748	0.0134	0.0389	0.0005	264.9	121.3	246.5	10.7	245.8	3.3

Table 2 (continued)

Spot	Th/U	Isotope ratio						Age (Ma)					
		$^{207}Pb/^{206}Pb$	± 1σ	$^{207}Pb/^{235}U$	± 1σ	$^{206}Pb/^{238}U$	± 1σ	$^{207}Pb/^{206}Pb$	± 1σ	$^{207}Pb/^{235}U$	± 1σ	$^{206}Pb/^{238}U$	± 1σ
12-ZG44-5	0.06	0.0529	0.0018	0.2865	0.0098	0.0390	0.0005	324.1	71.3	255.8	7.7	246.8	3.1
12-ZG44-6	0.11	0.0537	0.0018	0.2786	0.0092	0.0375	0.0004	366.7	75.9	249.6	7.3	237.2	2.7
12-ZG44-7	0.19	0.0498	0.0022	0.2540	0.0113	0.0367	0.0004	187.1	103.7	229.8	9.1	232.6	2.5
12-ZG44-8	0.09	0.0631	0.0022	0.3324	0.0133	0.0374	0.0004	710.8	74.1	291.4	10.1	236.5	2.5
12-ZG44-9	0.04	0.0508	0.0016	0.2643	0.0081	0.0375	0.0004	235.3	69.4	238.1	6.5	237.5	2.6
12-ZG44-10	0.07	0.0505	0.0013	0.2577	0.0067	0.0367	0.0004	220.4	56.5	232.8	5.4	232.6	2.2
12-ZG44-11	0.18	0.0494	0.0019	0.2509	0.0100	0.0368	0.0004	164.9	88.0	227.3	8.2	232.7	2.6
12-ZG44-12	0.13	0.0508	0.0021	0.2608	0.0108	0.0373	0.0005	231.6	62.0	235.3	8.7	235.9	2.9
12-ZG44-13	0.15	0.0508	0.0020	0.2605	0.0102	0.0372	0.0005	231.6	90.7	235.1	8.2	235.5	2.9
12-ZG44-14	0.04	0.0518	0.0018	0.2668	0.0095	0.0372	0.0004	279.7	84.2	240.2	7.6	235.2	2.7
12-ZG44-15	0.15	0.0484	0.0017	0.2517	0.0090	0.0375	0.0004	116.8	79.6	228.0	7.3	237.2	2.5
12-ZG44-16	0.09	0.0496	0.0016	0.2603	0.0084	0.0380	0.0004	176.0	78.7	234.9	6.7	240.4	2.4
Sample 12-ZG45, diorite porphyry dike													
ZG45-1	0.23	0.0485	0.0015	0.2502	0.0075	0.0370	0.0004	124.2	70.4	226.8	6.1	234.4	2.5
ZG45-2	0.24	0.0514	0.0016	0.2665	0.0085	0.0372	0.0004	257.5	72.2	239.9	6.8	235.3	2.4
ZG45-3	0.20	0.0522	0.0018	0.2717	0.0092	0.0376	0.0004	294.5	79.6	244.1	7.3	237.9	2.3
ZG45-4	0.44	0.0501	0.0020	0.2700	0.0105	0.0389	0.0004	198.2	92.6	242.7	8.4	246.3	2.4
ZG45-5	0.07	0.0522	0.0016	0.2669	0.0080	0.0370	0.0004	300.1	70.4	240.2	6.4	234.1	2.5
ZG45-6	0.21	0.0508	0.0018	0.2591	0.0089	0.0370	0.0004	227.8	81.5	233.9	7.2	233.9	2.7
ZG45-7	0.19	0.0531	0.0021	0.2720	0.0113	0.0368	0.0005	344.5	95.4	244.3	9.1	232.8	3.2
ZG45-8	0.26	0.0567	0.0021	0.2883	0.0107	0.0367	0.0004	479.7	86.1	257.3	8.4	232.2	2.5
ZG45-9	0.05	0.0507	0.0022	0.2618	0.0112	0.0374	0.0004	227.8	100.0	236.1	9.0	236.9	2.7
ZG45-10	0.16	0.0559	0.0020	0.2874	0.0100	0.0373	0.0004	455.6	81.5	256.5	7.9	236.1	2.5
ZG45-11	0.23	0.0516	0.0016	0.2629	0.0082	0.0365	0.0003	333.4	72.2	237.0	6.6	231.1	2.0
ZG45-12	0.21	0.0511	0.0015	0.2646	0.0079	0.0371	0.0004	242.7	75.0	238.4	6.4	235.1	2.5
ZG45-13	0.27	0.0627	0.0021	0.3233	0.0101	0.0371	0.0004	698.2	66.5	284.4	7.7	234.9	2.6
ZG45-14	0.18	0.0509	0.0018	0.2796	0.0099	0.0392	0.0005	235.3	81.5	250.4	7.8	248.0	2.8
ZG45-15	0.27	0.0546	0.0020	0.2962	0.0102	0.0388	0.0005	398.2	76.8	263.4	8.0	245.6	2.8
ZG45-16	0.16	0.0531	0.0018	0.2737	0.0088	0.0370	0.0004	331.5	77.8	245.7	7.0	234.2	2.6

zoning in some grains. Tiny apatite inclusions are sporadically observed in zircon grains and were avoided during subsequent U-Pb spot analyses as apatite may contain unusually high common Pb.

Eleven of 14 spot analyses of 14 zircon grains from the granodiorite dike (sample ZZG27) are concordant or nearly concordant, with $^{206}Pb/^{238}U$ dates ranging from 247.0 ± 3.6 Ma to 252.2 ± 3.1 Ma with a weighted mean of 248.9 ± 1.4 Ma (MSWD = 0.39; Fig. 9A). This date is considered to be the crystallization age of the granodiorite dike. The remaining three grains give older $^{206}Pb/^{238}U$ dates of 711.2 ± 28.2 Ma, 271.4 ± 3.4 Ma, and 272.0 ± 3.0 Ma (Table 2; Fig. 9A), and are interpreted to be inherited. Fourteen spot analyses of 14 zircon grains from the quartz diorite porphyry dike (sample ZA39) form a coherent group with a weighted mean $^{206}Pb/^{238}U$ date of 244.8 ± 1.4 Ma (MSWD = 1.11, Fig. 9B), which is interpreted to be the crystallization age of the quartz diorite porphyry dike.

Sixteen spot analyses were made on 16 zircons from the fresh diorite porphyry dike (sample 16-ZG306) that crosscuts a steeply-dipping, NE-striking gold orebody. Fifteen analyses have $^{206}Pb/^{238}U$ dates ranging from 233.0 ± 1.9 Ma to 243.4 ± 2.3 Ma, and yield a weighted mean $^{206}Pb/^{238}U$ date of 237.5 ± 1.4 Ma (MSWD = 1.3; Fig. 9C), which is considered to be the crystallization age of the diorite porphyry dike. The remaining one grain gives an older $^{207}Pb/^{206}Pb$ date of 250.5 ± 2.3 Ma (Table 2), and is interpreted to be inherited. Sixteen zircon grains from another diorite porphyry dike (sample 12-ZG42) have $^{206}Pb/^{238}U$ dates between 231.4 ± 2.1 Ma and 240.7 ± 3.1 Ma with a weighted mean of 236.2 ± 1.4 Ma (MSWD = 0.9; Fig. 9D) that is considered to be the crystallization age of the dike.

Two diorite porphyry dikes (samples 12-ZG44 and 12-ZG45) collected from the west part of the mining area yield identical zircon U-Pb ages. Twelve spot analyses on 12 zircon grains from sample 12-ZG44 are concordant and yield a weighted mean $^{206}Pb/^{238}U$ age of 235.7 ± 1.4 Ma (MSWD = 0.83; Fig. 9E). One spot analysis is discordant but has $^{206}Pb/^{238}U$ date indistinguishable from values of the 12 concordant analyses (Table 2), indicating that the discordance is likely caused by uncertainties of ^{207}Pb measurement. Thirteen zircon grains

from sample 12-ZG45 have similar $^{206}Pb/^{238}U$ dates, with a weighted mean of 234.5 ± 1.4 Ma (MSWD = 0.65; Fig. 9F). Of these, 10 spot analyses are concordant, and the other three are discordant with older $^{207}Pb/^{235}U$ dates. Two concordant spots from the sample 12-ZG44 together with the three discordant spots from the sample 12-ZG45 give older $^{206}Pb/^{238}U$ dates between 245.6 ± 2.8 Ma to 248.0 ± 2.8 Ma (Table 2), comparable to the U-Pb age of the granodiorite and quartz diorite porphyry dike samples and, thus, are considered to be inherited components.

8. Discussion

8.1. Timing of gold mineralization at Zaozigou

The U-Pb dates suggest that dikes in the Zaozigou mine were emplaced episodically in the 248.9 ± 1.4 to 234.5 ± 1.4 Ma interval. Field relationships between the dikes and gold mineralization place important constraints on the age of the Zaozigou deposit. In more detail, a granodiorite dike and a quartz diorite porphyry dike, which are cut by the NE-striking gold orebodies, have U-Pb ages of 248.9 ± 1.4 Ma (MSWD = 0.39; Fig. 9A) and 244.8 ± 1.4 Ma (MSWD = 1.11, Fig. 9B), respectively. Meanwhile, a fresh diorite porphyry dike that displaced an auriferous sericitized quartz diorite dike yielded a U-Pb age of 237.5 ± 1.4 Ma (MSWD = 1.3; Fig. 9C). These U-Pb ages bracket the age of gold mineralization to between 244.8 ± 1.4 Ma and 237.5 ± 1.4 Ma.

Field relationships and petrographic data show that both the sediment- and dike-hosted ores of the Zaozigou gold deposit are commonly associated with intense sericitization and silicification. Fluid inclusions in quartz veinlets intergrown with or overprinting the sericitic alteration have total homogenization temperatures ranging from 165.6° to 301.5 °C (Sanogo, 2008), which are below the closure temperature of argon isotopes in mica (350–300 °C; McDougall and Harrison, 1999). Thus, $^{40}Ar/^{39}Ar$ dates on sericite are likely to record the age of gold mineralization.
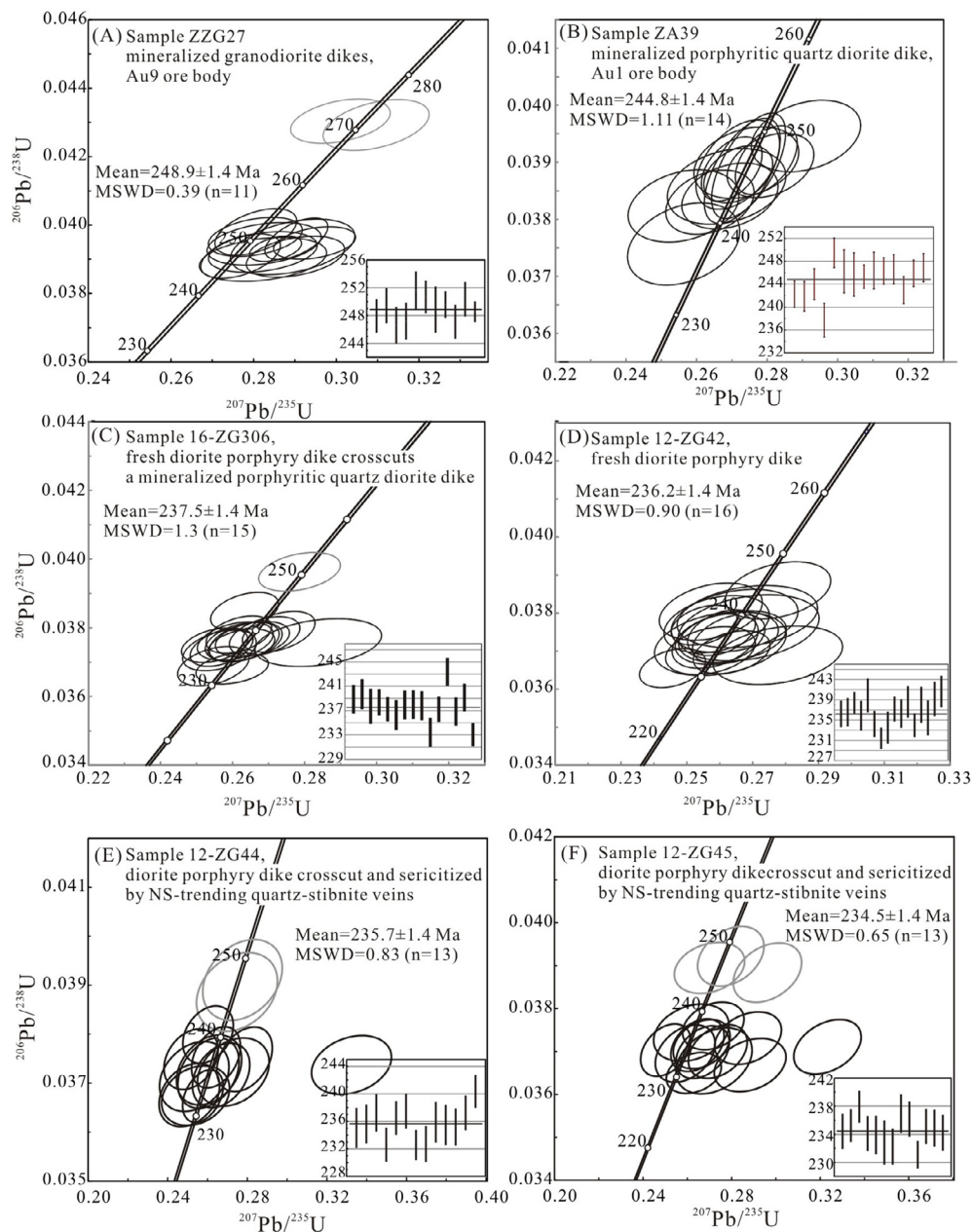
Fig. 9. Zircon U-Pb Concordia diagrams of various dikes in the mining area of the Zaozigou gold deposit.

The ⁴⁰Ar/³⁹Ar plateau age of sericite in sample ZG30 (245.6 ± 1.0 Ma; Fig. 8A) constrains the age of gold mineralization in the NE-striking gold orebodies. Within analytical uncertainty, this age is consistent with the zircon U-Pb age (244.8 ± 1.4 Ma; Fig. 9B) of an altered and mineralized quartz diorite porphyry dike (sample ZA39) that was cut by the NE-striking Au1 orebody (Fig. 5). These relationships suggest that the sericite ⁴⁰Ar/³⁹Ar plateau age is representative of gold deposition. The other sericite sample (ZG47) from sericitized siltstone-hosted ore in the NE-striking Au 1 orebody is about 3 Ma younger with a plateau age of 242.1 ± 1.2 Ma (Fig. 8B). If the 2 sigma analytical uncertainties are considered, the age difference of the two samples is 1.5 Ma. The apparent age difference may be explained in three ways: (1) hydrothermal activity lasted for 1.5–3 million years, (2) there were two separate hydrothermal events, or (3) sericite deposited at ca. 245.6 Ma was completely reset by post-ore magmatism at ca. 242 Ma. The second and third possibilities are consistent with development of many post-ore diorite porphyry dikes and the NW-trending, gently-dipping quartz-stibnite veins that crosscut and offset the gold

orebodies (Figs. 3, 4F and 5).

Collectively, our sericite ⁴⁰Ar/³⁹Ar and zircon U-Pb ages, combined with field relations, suggest that the subvertical NE- and NS-striking gold orebodies at Zaozigou formed soon after emplacement of quartz porphyry dikes between 245.6 ± 1.0 Ma and 242.1 ± 1.2 Ma. These orebodies are overprinted by later antimony-(gold) mineralization along dilatant N-S and NW-trending structures. Additional radiometric dating is needed to determine the age of antimony-(gold) mineralization.

8.2. Early to middle Triassic intrusion-related gold mineralization system in the Xiahe-Hezuo district

Geochronological data show that gold orebodies at Zaozigou formed at about 245–242 Ma, broadly coeval with the intermediate to felsic dike swarms in and surrounding the mining area. Gold mineralization with similar ages has also been recognized in the eastern zone of the Xiahe-Hezuo district. Hydrothermal biotite from the Dewulu Au-Cu

skarn deposit yielded a $^{40}Ar/^{39}Ar$ plateau age of 239.9 ± 1.4 Ma (2σ) that is identical to a zircon U-Pb age of 238.6 ± 1.5 Ma (2σ) of the Dewulu granitoid intrusion (Sui et al., 2017; Fig. 2). Although direct age dating of the Ayishan Cu-Au-(W) skarn deposit and the Jiangye'ang and Ka'ercha Au-As-Cu skarn deposits (Fig. 2) is lacking, the Ayishan and Xiahe granitoid plutons associated with those deposits have zircon U-Pb ages of 248–238 Ma (Jin et al., 2005; Wei et al., 2013; Xu et al., 2014). Hence, the majority of the gold-bearing skarn deposits in the eastern zone formed in the 248–238 Ma range. The Laodou gold deposit, hosted by the Laodou quartz diorite porphyry stock in the eastern zone (Fig. 2), consists of auriferous quartz-sulfide-tourmaline and minor quartz-stibnite veins (Jin et al., 2017). Hydrothermal sericites from the Laodou gold deposit have $^{40}Ar/^{39}Ar$ plateau ages of 249.1 ± 1.6 Ma and 249.0 ± 1.5 Ma (2σ) that are coeval with the age of the host intrusion (247.6 ± 1.3 Ma, 2σ; Jin et al., 2017). Taken together, our new $^{39}Ar/^{40}Ar$ and U-Pb ages combined with existing geochronological data demonstrate that magmatism and gold mineralization in the western and eastern zones of the Xiahe-Hezuo district were broadly coeval and occurred in the early to middle Triassic (ca. 248–238 Ma).

Although the genesis of the Zaozigou gold deposit has not been tightly constrained, the close spatial and temporal association between the gold orebodies and intermediate to felsic dike swarms implies a genetic connection. This view is partly confirmed by the magmatic origin of the gold deposits in the eastern zone that have the same age as Zaozigou. For example, the H-O isotopic composition of sericite and the H-O-B isotopic composition of tourmaline from the Laodou gold deposit are indicative of a magmatic source for the ore-forming fluids (Jin et al., 2017). Simialrly, the abundance of Au-Cu-(W) skarn deposits shows that the early to middle Triassic granitoid magmas were enriched in gold and copper. The early to middle Triassic granitoid intrusions in the Xiahe-Hezuo district, including the ore-related Dewulu and Laodou intrusions, are ilmenite-series granitoids (Jin et al., 2017; Sui et al., 2017). The granodiorite and quartz diorite porphyry dikes at Zaozigou have accessory minerals, including zircon, apatite, ilmenite, and titanite, that are consistent with ilmenite-series granites (Ishihara, 1981). Thus, we infer that magmas in the western and eastern zones were derived from the same or very similar magmatic sources. Volatiles exsolved from such reduced magmas are the most likely source of fluids that formed the Zaozigou gold deposit and the Au veins and Au-Cu skarns in the eastern zone. Sediment- and dike-hosted gold deposits (Fig. 2) in the western zone are likely the shallow products of the deep-seated magmatic-hydrothermal gold system exposed in the eastern zone (e.g., gold skarn and intrusion-related gold). Although Triassic sedimentary rocks and sediment-hosted gold deposits may also have been present in the eastern zone, they were eroded away following uplift of the eastern zone along the Xiahe-Lintan fault.

8.3. Tectonic setting of the early to middle Triassic gold mineralization

The numerous early-middle Triassic granitoid plutons with small amounts of andesite to dacite (242–234 Ma; Guo et al., 2012; Li et al., 2013) on the northwestern margin of the West Qinling orogen have geochemical signatures (e.g., LILE and LREE enrichment, HFSE depletion, high $Mg^{\#}$) typical of an active continental margin arc (Hawkesworth et al., 1993; Pearce, 1983). The high $Mg^{\#}$ values of (> 50; Li et al., 2015b; Luo et al., 2015) and abundant mafic microgranular enclaves in these granitoid intrusions suggest that they are hybrid products of mafic and felsic melts (Li et al., 2015b; Luo et al., 2015). The mafic melts are likely equivalents of the gabbro and gabbroic diorite phases of the Gangcha intrusive complex in the Tongren district to the west of Xiahe-Hezuo district, which are coeval with the granitoids investigated in this study (zircon U-Pb ages of 243.8 ± 1.0 to 234.0 ± 0.6 Ma; Guo et al., 2012; Luo et al., 2012). Such evidence implies that mafic magmatism accompanied granitoid magmatism at ca. 250–230 Ma and has been attributed to partial melting of

lithospheric mantle due to lithospheric extension triggered by asthenospheric upwelling (Huang et al., 2014).

Several mechanisms have been proposed to explain the Triassic lithospheric extension and associated magmatism in the Xiahe-Hezuo district and large areas to the northwest: slab break-off (Luo et al., 2015, 2012; Zhang et al., 2007), lithosphere delamination (Zhang et al., 2008) in post-collisional setting, and slab retreat in an active continental margin setting (Huang et al., 2014; Li et al., 2015b, 2013). The small amounts of andesite to dacite (242–234 Ma; Guo et al., 2012; Li et al., 2013) in those areas are characterized by LILE and LREE enrichment, HFSE depletion and high Mg #, which is typical of active continental margin magmatic arcs (Hawkesworth et al., 1993; Pearce, 1983). Paleomagnetic data also suggest that continental collision between the North China and South China Blocks did not occur before middle-late Triassic (Enkin et al., 1992; Hacker et al., 2004). In addition, the huge thickness (> 10 km) of lower-middle Triassic turbiditic deposits in the western portion of the West Qinling orogen and Songpan-Ganze basin (inset of Fig. 1) indicate that the Animaque ocean survived and its northward subduction did not cease until the Ladinian (237–229 Ma; Meng et al., 2005). The transition from Late Permian–Early Triassic proximal slope facies strata to base-of-slope fan sediments by the Middle Triassic has been interpreted to record the opening of a continental margin back-arc basin in the northern part of the West Qinling (Li et al., 2014a). Together, the aforementioned evidence suggests that the western segment of the West Qinling orogen evolved in a subduction-related regime during the early-middle Triassic. The lithospheric extension and associated magmatism and gold mineralization in this setting was likely in response to rollback of the subducted paleo-Tethyan oceanic slab (Li et al., 2014b, 2015b).

8.4. Comparison with vein gold deposits in the eastern segment of the West Qinling orogen

In the eastern segment of the West Qinling orogen, gold deposits hosted in Devonian greenschist-facies metasedimentary rocks (e.g., Shuangwang, Baguamiao, Liba, Ma'anqiao; Fig. 1) are associated with NNW-trending brittle–ductile shear zones, which are secondary or higher-order structures of regional thrusts. These deposits are characterized by auriferous quartz veins and disseminated mineralization in altered, locally brecciated, Paleozoic metasedimentary rocks along shear zones. Sulfide minerals in these gold deposits mainly consist of pyrite with minor amounts of arsenopyrite, pyrrhotite, galena, sphalerite, and chalcopyrite. Compared to the gold deposits in the Xiahe-Hezuo district, a striking feature of those deposits is the ductile to ductile-brittle character of the ore-hosting structures and the absence of coeval skarn type gold mineralization. A structural reconstruction suggests that large-scale south-directed thrusting and folding in eastern segment of the West Qinling orogen occurred during the Carnian and Norian time of the late Triassic epoch in response to continental collision between the North and South China blocks (Li et al., 1999; Wu et al., 2014). Recent high precision geochronological studies on several gold deposits in the eastern segment of West Qinling (e.g. Liba and Huachanggou) show that gold mineralization occurred in the Norian from 216 to 210 Ma (Fig. 10D; Zeng et al., 2012; Zhou et al., 2014), which is 30–40 Ma younger than the gold deposits in the Xiahe-Hezuo district (Fig. 10C).

Such an age difference is also observed between granitoid intrusions in the eastern and western segments of the West Qinling orogen (Fig. 10A and B). Subduction-related plutonic-volcanic complexes were emplaced in the 253–234 Ma interval along the northern margin of the western segment of the West Qinling orogen (Fig. 10A). In contrast, granitic plutons and numerous dikes in the eastern segment of the West Qinling were emplaced between 237 and 203 Ma (Fig. 10B). The younger period of magmatism is less significant in the western segment (Fig. 10A). According to their age and composition, the younger granitoid intrusions have been further divided into syn-collisional
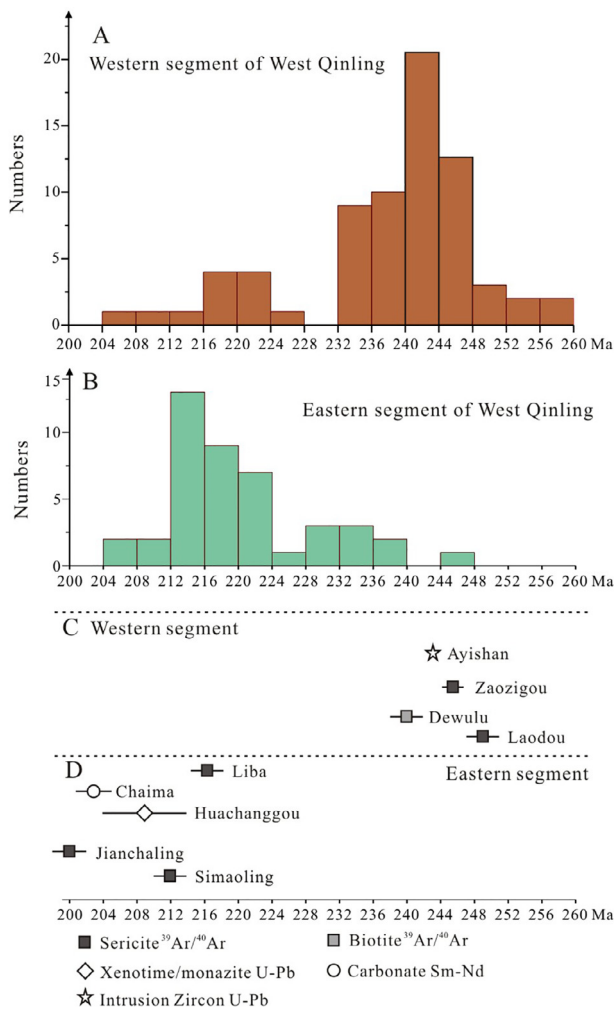
Fig. 10. A. Histogram of Zircon U-Pb ages of granitoid intrusions, volcanic rocks and mafic-ultramafic intrusions in the western segment of West Qinling orogen, data are from Guo et al. (2012), Han et al. (2014), Huang et al. (2014), Jin et al. (2005), Kou et al. (2009), Li et al. (2013; 2014b), Liu et al. (2012), Luo (2013), Wang et al. (2010), Wei et al. (2013), Xu et al. (2014), Yang et al. (2015a) and Zhang et al. (2006). B. Age distribution of granitoid intrusions in the eastern segment of West Qinling orogen, data are from Huang et al. (2013b), Li et al. (2015a), Liu and Li (2012), Ren et al. (2014), Sun et al. (2002), Yang et al.(2014, 2015b), Zeng et al. (2014) and Zhu et al.(2013, 2011). C. D. Isotopic ages of representative gold deposits in the western and eastern part of West Qinling orogen, data are from Jin et al. (2017), Liu et al. (2014), Sui et al. (2017), Wang et al. (2014), Zeng et al. (2012) and Zhou et al. (2014).

(237–210 Ma) and post-collisional (210–203 Ma) groups (Dong et al., 2015, 2011). Based on above data, we suggest that gold mineralization in the eastern and western segments of the West Qinling orogen occurred diachronously in different tectonic settings. The early to middle Triassic gold mineralization in the western segment of the West Qinling orogen was mainly associated with subduction-related magmatism whereas the late Triassic gold mineralization in the eastern segment formed in a syn- or post-collisional setting and was mainly due to metamorphic devolatization. However, we acknowledge that minor gold and antimony deposits of late Triassic age are also present in the western segment.

9. Conclusions

The Zaozigou sediment- and dike-hosted gold deposit in the western zone of the Xiahe-Hezuo district consists of sediment-hosted gold mineralization with minor auriferous sulfide-quartz-ankerite veinlets that

are controlled by subvertical NE- and NS-trending faults. The gold orebodies are overprinted by stibnite-(gold)-quartz veins or stockworks localized along NW-striking, gently-dipping faults and reactivated NS-trending faults. Zircon U-Pb dates on pre- and post-ore dikes bracket the timing of gold mineralization to 245–237 Ma. $^{40}Ar/^{39}Ar$ plateau dates on ore-related sericite constrain the age of hydrothermal alteration and gold deposition to 245–242 Ma. The close spatial and temporal association between the gold orebodies and ilmenite-series dike swarms in the western zone, together with the coeval Au-Cu skarns, intrusion-related gold vein deposits and early-middle Triassic ilmenite series intrusions in the eastern zone, suggest that Zaozigou is a shallow expression of a reduced intrusion-related gold system. Gold mineralization in the Xiahe-Hezuo district formed in an extensional back-arc setting presumably associated with rollback of the subducted paleo-Tethyan slab during the early to middle Triassic. In contrast, gold deposits in the eastern segment of West Qinling orogen formed in the late Triassic during continental collision between the North and South China blocks. Thus, the large endowment of gold in the West Qinling orogen was produced by the combined effects of metallogenic events associated with early-middle Triassic subduction and late Triassic continental collision.

Appendix A. Supplementary data

Supplementary data associated with this article can be found, in the online version, at https://doi.org/10.1016/j.oregeorev.2018.08.014.

References

Cao, X.F., Sanogo, M.L.S., Lv, X.B., He, M.C., Chen, C., Zhu, J., Tang, R.K., Liu, Z., Zhang, B., 2012. Ore-forming process of the zaozigou gold deposit: constraints from geological characteristics, gold occurrence and stable isotope compositions. J. Jilin Univ. (Earth Sci. Ed.) 42 (4), 1039–1054 in Chinese with English abstract.

Chen, G.Z., Liang, Z.L., Wang, J.L., Li, P.B., Ma, H.S., Zhang, Y.N., 2015. The variation pattern of gold grade of the zaozigou gold deposit. Miner. Deposits 34 (1), 149–162 in Chinese with English abstract.

Chen, Y.Y., Luo, X.G., Li, W.J., 2011. Overview of gold exploration in Gansu area during the eleventh five-year plan. Geol. Gansu 20 (4), 5–12 in Chinese with English abstract.

Chen, Y.J., Santosh, M., 2014. Triassic tectonics and mineral systems in the Qinling Orogen, central China. Geol. J. 49, 338–358.

Chen, Y.J., Zhang, J., Zhang, F.X., Pirajno, F., Li, C., 2004. Carlin and carlin-like gold deposits in western Qinling mountains and their metallogenic time, tectonic setting and model. Geol. Rev. 50 (2), 134–152 in Chinese with English abstract.

Corfu, F., Hanchar, J.M., Hoskin, P., Kinny, P., 2003. Atlas of zircon textures. Rev. Mineral. Geochem. 53 (1), 469–500.

Deino, A., Potts, R., 1990. Single crystal $^{40}Ar/^{39}Ar$ dating of the olorgesailie formation, Southern Kenya Rift. J. Geophys. Res. Sol. Ea. 95 (B6), 8453–8470.

Dong, Y.P., Zhang, G.W., Neubauer, F., Liu, X.M., Genser, J., Hauzenberger, C., 2011. Tectonic evolution of the Qinling orogen, China: review and synthesis. J. Asian Earth Sci. 41 (3), 213–237.

Dong, Y., Zhang, X., Liu, X., Li, W., Chen, Q., Zhang, G., Zhang, H., Yang, Z., Sun, S., Zhang, F., 2015. Propagation tectonics and multiple accretionary processes of the Qinling Orogen. J. Asian Earth Sci. 104, 84–98.

Enkin, R.J., Yang, Z., Chen, Y., Courtillot, V., 1992. Paleomagnetic constraints on the geodynamic history of the major blocks of China from the Permian to the present. J. Geophys. Res. Sol. Ea. 97 (B10), 13953–13989.

Feng, Y.M., Cao, X.D., Zhang, E.P., 2002. In: The Structure, Orogenic Process and

Dynamics of West Qinling Orogenic Belt. Xi'an Map Press, Xi'an, pp. 1–263 in Chinese.

Guo, X.Q., Yan, Z., Wang, Z.Q., Wang, T., Hou, K.J., Fu, C.L., Li, J.L., 2012. Middle Triassic arc magmatism along the northeastern margin of the Tibet: U-Pb and Lu-Hf zircon characterization of the Gangcha complex in the West Qinling terrane, central China. J. Geol. Soc. London 169 (3), 327–336.

Hacker, B.R., Ratschbacher, L., Liou, J.G., 2004. Subduction, collision and exhumation in the ultrahigh-pressure Qinling-Dabie orogen. Geol. Soc. London Spec. Publ. 226 (1), 157–175.

Han, J., Yao, J., Chen, Y., 2014. Geochronology and geochemistry of the Dashui adakitic granitoids in the western Qinling Orogen, central China: implications for Triassic tectonic setting. Geol. J. 49 (4–5), 383–401.

Hawkesworth, C.J., Gallagher, K., Hergt, J.M., McDermott, F., 1993. Mantle and slab contribution in arc magmas. Annu. Rev. Earth Planet Sci. 21, 175–204.

Huang, X.F., Mo, X.X., Yu, X.H., Li, X.W., Ding, Y., Wei, P., He, W.Y., 2013b. Zircon U-Pb chronology, geochemistry of the Late Triassic acid volcanic rocks in Tanchang area, West Qinling and their geological significance. Acta Petrol. Sin. 29 (11), 3968–3980 in Chinese with English abstract.

Huang, X., Yu, X., Mo, X., Li, X., Ding, Y., Wei, P., He, W., Yu, J., 2013a. The discovery of OIB-type potassic tholeiitic basalts from the Ganjia area in West Qinling: implications for the Late Mesozoic continental rift of West Qinling. Earth Sci. Front. 20 (3), 204–216 In Chinese with English abstract.

Huang, X., Mo, X., Yu, X., Li, X., Yang, M., Luo, M., He, W., Yu, J., 2014. Origin and geodynamic settings of the Indosinian high Sr/Y granitoids in the West Qinling: an example from the Shehaliji pluton in Tongren area. Acta Petrol. Sin. 30 (11), 3255–3270 in Chinese with English abstract.

Ishihara, S., 1981. The granitoid series and mineralization. Economic Geology 75th Anniversary Volume, pp. 458–484.

Jiang, Y., Jin, G., Liao, S., Zhou, Q., Zhao, P., 2010. Geochemical and Sr-Nd-Hf isotopic constraints on the origin of Late Triassic granitoids from the Qinling orogen, central China: implications for a continental arc to continent-continent collision. Lithos 117 (1–4), 183–197.

Jin, X., Li, J., Hofstra, A.H., Sui, J., 2017. Magmatic-hydrothermal origin of the early Triassic Laodou lode gold deposit in the Xiahe-Hezuo district, West Qinling orogen, China: implications for gold metallogeny. Miner. Deposita 52 (6), 883–902.

Jin, W.J., Zhang, Q., He, D.F., Jia, X.Q., 2005. SHRIMP dating of adakites in western Qinling and their implications. Acta Petrol. Sin. 21 (3), 959–966 in Chinese with English abstract.

Kou, X.H., Zhang, K.X., Zhu, Y.H., Chen, Z.Q., Lin, Q.X., Chen, F.N., Huang, J.Y., 2009. Middle Permian Seamount from Xiahe Area, Gansu Province, Northwest China: zircon U-Pb Age, Biostratigraphy and Tectonic Implications. J. Earth Sci. China 20 (02), 364–380.

Kröner, A., Zhang, G.W., Sun, Y., 1993. Granulites in the Tongbai area, Qinling belt, China: geochemistry, petrology, single zircon geochronology, and implications for the tectonic evolution of eastern Asia. Tectonics 12 (1), 245–255.

Kuiper, K.F., Deino, A., Hilgen, F.J., Krijgsman, W., Renne, P.R., Wijbrans, J.R., 2008. Synchronizing rock clocks of earth history. Science 320 (5875), 500–504.

Li, N., Chen, Y., Santosh, M., Pirajno, F., 2015a. Compositional polarity of Triassic granitoids in the Qinling Orogen, China: implication for termination of the northernmost paleo-Tethys. Gondwana Res. 27 (1), 244–257.

Li, L., Meng, Q., Pullen, A., Garzione, C.N., Wu, G., Wang, Y., Ma, S., Duan, L., 2014a. Late Permian-early Middle Triassic back-arc basin development in West Qinling. China. J. Asian Earth Sci. 87, 116–129.

Li, X., Mo, X., Yu, X., Ding, Y., Huang, X., Wei, P., He, W., 2013. Petrology and geochemistry of the early Mesozoic pyroxene andesites in the Maixiu Area, West Qinling, China: products of subduction or syn-collision? Lithos 172–173, 158–174.

Li, X., Mo, X., Bader, T., Scheltens, M., Yu, X., Dong, G., Huang, X., 2014b. Petrology, geochemistry and geochronology of the magmatic suite from the Jianzha Complex, central China: petrogenesis and geodynamic implications. J. Asian Earth Sci. 95, 164–181.

Li, X., Mo, X., Huang, X., Dong, G., Yu, X., Luo, M., Liu, Y., 2015b. U-Pb zircon geochronology, geochemical and Sr-Nd-Hf isotopic compositions of the Early Indosinian Tongren Pluton in West Qinling: petrogenesis and geodynamic implications. J. Asian Earth Sci. 97, 38–50.

Li, J., Wang, Z., Zhao, M., Abbott, E.W., 1999. ^{40}Ar/^{39}Ar thermochronological constraints on the timing of collisional orogeny in the Mianlue collision belt, Southern Qinling mountains. Acta Geol. Sin. Engl. 73 (02), 208–215.

Liu, X.L., Wang, Y.T., Hu, Q.Q., Wei, R., Wang, R.T., Wen, S.W., Chen, M.S., Yang, G.H., 2014. Sm-Nd isotopic dating of carbonate minerals from the Chaima gold deposit in the Fengxian-Taibai ore concentration area, Shaanxi Province and its implications. Acta Petrol. Sin. 30 (1), 271–280.

Liu, Y., Hu, Z., Gao, S., Günther, D., Xu, J., Gao, C., Chen, H., 2008. In situ analysis of major and trace elements of anhydrous minerals by LA-ICP-MS without applying an internal standard. Chem. Geol. 257 (1), 34–43.

Liu, J.P., Lai, J.Q., Gu, X.P., Wang, X.J., Mao, Y., Song, W.B., 2012. Geochemistry and zircon LA-ICPMS U-Pb geochronology of intrusive body in Saishitang copper deposit, Qinghai province, China. Chin. J. Nonferrous Metals 03, 622–632 in Chinese with English abstract.

Liu, C.X., Li, L., Sui, J.X., 2011. Mineralization characteristics and ore genesis of the zaozigou gold deposit, Gansu Province. Geol. Sci. Tech. Inf. 30 (6), 66–74 in Chinese with English abstract.

Liu, Z.P., Li, J.W., 2012. Magma mixing genesis of the Jinchang quartz diorite in West Qinling orogen, Western China: petrographical and geochronological constraints and their tectonic implications. Acta Geol. Sin. 86 (7), 1077–1090 in Chinese with English abstract.

Liu, J., Liu, C., Carranza, E.J.M., Li, Y., Mao, Z., Wang, J., Wang, Y., Zhang, J., Zhai, D.,

Zhang, H., Shan, L., Zhu, L., Lu, R., 2015. Geological characteristics and ore-forming process of the gold deposits in the western Qinling region, China. J. Asian Earth Sci. 103, 40–69.

Liu, D.S., Tan, Y.J., Wang, J.Y., Wei, L.M., 1994. Carlin-type gold deposits in China. In: Liu, D.S., Tan, Y.J., Wang, J.Y. (Eds.), Chinese Carlin-type Gold Deposits. Nanjing University Press, Nanjing, pp. 1–38 in Chinese.

Ludwig, K.R., 2003. Isoplot/Ex version 3.00: a geochronological toolkit for Microsoft Excel. Berkeley geochronology center. Spec. Publ. 4, 1–73.

Luo, B.J., Zhang, H.F., Lu, X.B., 2012. U-Pb zircon dating, geochemical and Sr-Nd-Hf isotopic compositions of Early Indosinian intrusive rocks in West Qinling, central China: petrogenesis and tectonic implications. Contrib. Mineral. Petrol. 164 (4), 551–569.

Luo, B., Zhang, H., Xu, W., Guo, L., Pan, F., Yang, H., 2015. The Middle Triassic Meiwu batholith, West Qinling, central China: implications for the evolution of compositional diversity in a composite batholith. J. Petrol. 56 (6), 1139–1172.

Luo, B.J., 2013. Petrogenesis and Geodynamic Processes of The Indosinian Magmatism In The West Qinling Orogenic Belt, Central China. Ph. D. Thesis. China University of Geosciences, Wuhan, China, pp. 191 in Chinese with English abstract.

Mao, J.W., Qiu, Y.M., Goldfarb, R.J., Zhang, Z.C., Garwin, S., Ren, F.S., 2002. Geology, distribution, and classification of gold deposits in the western Qinling belt, central China. Miner. Deposita 37 (3–4), 352–377.

McDougall, I., Harrison, T.M., 1999. In: Geochronology and Thermochronology by the ^{40}Ar/^{39}Ar Method. Oxford University Press, New York, pp. 263.

Meng, Q.R., Wang, E., Hu, J.M., 2005. Mesozoic sedimentary evolution of the northwest Sichuan basin: Implication for continued clockwise rotation of the South China block. Geol. Soc. Am. Bull. 117 (3–4), 396–410.

Meng, Q.R., Zhang, G.W., 2000. Geologic framework and tectonic evolution of the Qinling orogen, central China. Tectonophysics 323 (3–4), 183–196.

Pearce, J.A., 1983. Role of the sub-continental lithosphere in magma genesis at active continental margins. In: Hawkesworth, C.J., Norry, M.J. (Eds.), Continental Basalts and Mantle Xenoliths. Shiva Publications, Nantwich, Cheshire, pp. 230–249.

Qin, J., Lai, S., Grapes, R., Diwu, C., Ju, Y., Li, Y., 2009. Geochemical evidence for origin of magma mixing for the Triassic monzonitic granite and its enclaves at Mishuling in the Qinling orogen (central China). Lithos 112 (3–4), 259–276.

Ren, H.Z., Pei, X.Z., Liu, C.J., Li, Z.C., Li, R.B., Wei, B., Chen, W.N., Wang, Y.Y., Xu, X.C., Liu, T.J., Chen, Y.X., 2014. LA-ICP-MS zircon U-Pb dating and geochemistry of the Taibai intrusion in Tianshui areas of western Qinling Mountains and their geological significance. Geol. Bull. China 33 (7), 1041–1054 in Chinese with English abstract.

Renne, P.R., Cassata, W.S., Morgan, L.E., 2009. The isotopic composition of atmospheric argon and ^{40}Ar/^{39}Ar geochronology: Time for a change? Quat. Geochronol. 4 (4), 288–298.

Sanogo, M.L.S., 2008. Structural, Fluid and Geochemical control of Zaozigou Gold Deposit, Gansu, China. M. Sc. Thesis. China University of Geosciences, Wuhan, pp. 98.

Steiger, R.H., Jäger, E., 1977. Subcommission on geochronology: convention on the use of decay constants in geo-and cosmochronology. Earth Planet. Sc. Lett. 36 (3), 359–362.

Sui, J., Li, J., Wen, G., Jin, X., 2017. The Dewulu reduced Au-Cu skarn deposit in the Xiahe-Hezuo district, West Qinling orogen, China: implications for an intrusion-related gold system. Ore Geol. Rev. 80, 1230–1244.

Sui, J.X., 2016. The Reduced Intrusion-Related Gold Mineralization in the Xiahe-Hezuo District, West Qinling Orogeny. Ph. D. Thesis. China University of Geosciences, Wuhan, pp. 182.

Sun, W.D., Li, S.G., Chen, Y.D., Li, Y.J., 2002. Timing of synorogenic granitoids in the South Qinling, central China: constraints on the evolution of the Qinling-Dabie orogenic belt. J. Geol. 110 (4), 457–468.

Vasconcelos, P.M., Onoe, A.T., Kawashita, K., Soares, A.J., Teixeira, W., 2002. ^{40}Ar/^{39}Ar geochronology at the Instituto de Geociências, USP: instrumentation, analytical procedures, and calibration. Anais da Academia Brasileira de Ciências 74 (2), 297–342.

Wang, Y.T., Li, X., Wang, R.T., Liu, X.L., Hu, Q.Q., Li, J.H., Wang, C.A., Wen, B., Wen, S.W., Wang, S.L., 2014. Evidence of Ar-Ar Age for the metallogenic epoch of simaoling gold deposit in Fengxian-Taibai ore cluster of Shaanxi. J. Earth Sci. Environ. 36 (3), 61–72 in Chinese with English abstract.

Wang, Z.P., Yang, F.Q., Zhao, P.R., 1995. The feature and evolution of Permian rift of Qinling orogenic belt. Earth Sci. 20 (6), 631–640 in Chinese with English abstract.

Wang, H.Q., Zhu, Y.H., Lin, Q.X., Li, Y.L., Wang, K., 2010. LA-ICP-MS zircon U-Pb dating of the gabbro from Longwu Gorge ophiolite, Jianzha-Tongren area, Qinghai, China and its geological significance. Geol. Bull. China 1 (29), 86–92 in Chinese with English abstract.

Wei, L.X., Chen, Z.L., Pang, Z.S., Han, F.B., Xiao, C.H., 2018. An Analysis of the Tectonic Stress Field in the Zaozigou Gold Deposit, Hezuo Area, Gansu Province. Acta Geosci. Sin. 39 (01), 1–15 in Chinese with English abstract.

Wei, P., Mo, X., Yu, X., Huang, X., Ding, Y., Li, X., 2013. Geochemistry, chronology and geological significance of the granitoids in Xiahe, West Qinling. Acta Petrol. Sin. 29 (11), 3981–3992 in Chinese with English abstract.

Wu, G., Meng, Q., Duan, L., Li, L., 2014. Early Mesozoic structural evolution of the eastern West Qinling, northwest China. Tectonophysics 630, 9–20.

Xu, X.Y., Chen, J.L., Gao, T., Li, P., Li, T., 2014. Granitoid magmatism and tectonic evolution in northern edge of the Western Qinling terrane, NW China. Acta Petrol. Sin. 30 (2), 371–389 in Chinese with English abstract.

Yang, P., Liu, S., Li, Q., Wang, Z., Zhang, F., Wang, W., 2014. Chronology and petrogenesis of the Hejiazhuang granitoid pluton and its constraints on the Early Triassic tectonic evolution of the South Qinling Belt. Sci. China Ser. D Earth Sci. 57 (2), 232–246 in Chinese with English abstract.

Yang, Y., Wang, X.X., Ke, C.H., Wang, S.A., Li, J.B., Nie, Z.R., Lv, X.Q., 2015b. Zircon U-Pb ages and petrogenesis of the Luchuba pluton in West Qinling and its geological

significance. Acta Geol. Sin. 10, 1735–1761 in Chinese with English abstract.

Yang, G., Yang, S., Wei, L., Li, Z., Li, R., Xu, D., Liu, M., 2015a. Petrogenesis and geodynamic significance of the Late Triassic Tadong adakitic pluton in West Qinling, central China. Int. Geol. Rev. 57 (13), 1755–1771.

Yin, H.F., Yang, F.Q., Huang, Q., Yang, H.S., Lai, X.L., 1992. In: The Triassic of Qinling Mountains and Neighboring Areas. China University of Geosciences Press, Wuhan, pp. 1–211 in Chinese.

Zeng, Q.T., McCuaig, T.C., Hart, C., Jourdan, F., Muhling, J., Bagas, L., 2012. Structural and geochronological studies on the Liba goldfield of the West Qinling Orogen, Central China. Miner. Deposita 47 (7), 799–819.

Zeng, Q., Mccuaig, T.C., Tohver, E., Bagas, L., Lu, Y., 2014. Episodic Triassic magmatism in the western South Qinling Orogen, central China, and its implications. Geol. J. 49 (4–5), 402–423.

Zhang, H.F., Chen, Y.L., Xu, W.C., Liu, R., Yuan, H.L., Liu, X.M., 2006. Granitoids around Gonghe basin in Qinghai province: petrogenesis and tectonic implications. Acta Petrol. Sin. 22 (12), 2910–2922 in Chinese with English abstract.

Zhang, G.W., Dong, Y.P., Lai, S.C., Guo, A.L., Meng, Q.R., Liu, S.F., Cheng, S.Y., Yao, A.P., Zhang, Z.Q., Pei, X.Z., Li, S.Z., 2004. Mianlue tectonic zone and Mianlue suture zone on southern margin of Qinling-Dabie orogenic belt. Sci. China Ser. D Earth Sci. 47 (4), 300–316 in Chinese with English abstract.

Zhang, G.W., Zhang, B.R., Yuan, X.C., Xiao, Q.H., 2001. In: Qinling Orogenic Belt and Continental Dynamics. Science Press, Beijing, pp. 1–729 in Chinese.

Zhang, H.F., Jin, L.L., Zhang, L., Harris, N., Zhou, L., Hu, S.H., Zhang, B.R., 2007. Geochemical and Pb-Sr-Nd isotopic compositions of granitoids from western Qinling belt: constraints on basement nature and tectonic affinity. Sci. China Ser. D Earth Sci. 50 (2), 184–196.

Zhang, G.W., Meng, Q.R., Zhou, D.W., Guo, A.L., 1996. Orogenesis and dynamics of the Qinling orogen. Sci. China Ser. D Earth Sci. 39, 225–239 in Chinese with English abstract.

Zhang, C.L., Wang, T., Wang, X.X., 2008. Origin and tectonic setting of the early Mesozoic granitoids in Qinling orogenic belt. Geol. J. China Univ. 14 (3), 304–316 in Chinese with English abstract.

Zhao, J.T., Yang, F.Q., 1992. Permian sedimentary features and environmental analysis of Maomaolong Formation in Malonggou, Xiahe, Gansu. Acta Sedimentol. Sin. 10 (1), 47–56 in Chinese with English abstract.

Zhou, Z., Lin, Z., Qin, Y., 2014. Geology, geochemistry and genesis of the Huachanggou gold deposit, western Qinling Orogen, central China. Geol. J. 49 (4–5), 424–441.

Zhu, L.M., Zhang, G.W., Chen, Y.J., Ding, Z.J., Guo, B., Wang, F., Lee, B., 2011. Zircon U-Pb ages and geochemistry of the Wenquan Mo-bearing granitoids in West Qinling, China: constraints on the geodynamic setting for the newly discovered Wenquan Mo deposit. Ore Geol. Rev. 39 (1–2), 46–62.

Zhu, L., Zhang, G., Yang, T., Wang, F., Gong, H., 2013. Geochronology, petrogenesis and tectonic implications of the Zhongchuan granitic pluton in the Western Qinling metallogenic belt. China. Geol. J. 48 (4), 310–334.